1 **Ambient and Intrinsic Dependencies of Evolving Ice-Phase Particles within a Decaying**

2 **Winter Storm During IMPACTS**

5 *Andrew DeLaFrance[1,a], Lynn A. McMurdie[1], Angela K. Rowe[2], Andrew J. Heymsfield[3,4]*

8 [1]Department of Atmospheric and Climate Science, University of Washington, Seattle, WA, USA

9 [2]Department of Atmospheric and Oceanic Sciences, University of Wisconsin-Madison, Madison, WI, USA

10 [3]National Center for Atmospheric Research, Boulder, CO, USA

11 [4]US National Science Foundation, Alexandria, VA, USA

12 [a]now at: Institute for Atmospheric and Environmental Research, University of Wuppertal, Wuppertal, Germany

15 *Submitted to EGU Atmospheric Chemistry and Physics*

16 *3 November 2024*

17 *Revised manuscript submitted 27 March 2025*

20 Corresponding author: Andrew DeLaFrance, delafrance@uni-wuppertal.deadelaf@uw.edu

28 **Abstract**

29   Mesoscale bands develop within winter cyclones as concentrated regions of locally enhanced

30 radar reflectivity, often ~~producing~~ corresponding to intensified precipitation rates lasting several

31 hours. Surface precipitation characteristics are governed by the microphysical properties of the

32 ice-phase particles aloft, yet their unique microphysical evolutionary pathways and ambient

33 environmental dependencies in banded regions remain poorly understood, in part due to a

34 paucity of observations within ~~natural~~ clouds. Addressing this need, the Investigation of

35 Microphysics and Precipitation for Atlantic Coast-Threatening Snowstorms ~~recently~~ measured

36 properties of winter cyclones from airborne in situ and remote sensing platforms. Observations

37 collected within a banded region of a decaying-stage northeast United States cyclone revealed a

38 microphysical pathway characterized by precipitation fallout from a weak generating cell layer

39 through an ~2 km deep subsaturated downdraft region. Sublimation was a dominant evolutionary

40 process, resulting in > 70% reduction of the initial characteristic ice water content (IWC). This

41 vertical evolution was reproduced by a 1D particle-based model simulation constrained by

42 observations, conveying accuracy in the process representation. Four sensitivity simulations

43 assessed evolutionary dependencies based on observationally-informed perturbations of the

44 ambient relative humidity, RH, and vertical air motion, w. Perturbations of ~2% RH significantly

45 varied the resultant characteristic IWC loss, as much as 29%, whereas comparable perturbations

46 of w had negligible effects. Intrinsic particle evolution during sublimation demonstrated a

47   notable imprint on vertical profiles of radar reflectivity, but Doppler velocity was more strongly

48   governed by the ambient w profile. These findings contextualize radar-based discrimination of

49   sublimation from other ice-phase processes, including riming and aggregation.

50   **1. Introduction**

51   ~~The microphysical pathways for precipitation evolution within winter storms are uniquely~~

52 ~~dependent on physical properties of the storm across synoptic to microscales that vary~~

53 ~~temporally and spatially. Consequently, winter storms exhibit significant heterogeneities in~~

54 ~~precipitation intensity and distribution.~~ Northeast U.S. winter cyclones commonly develop

55 mesoscale banded regions which can produce intense rain- and snowfall rates within

56 concentrated regions of the storm (Novak et al., 2004, 2008; Ganetis et al., 2018). These

57 mesoscale bands ~~are readily~~ may be diagnosed from ~~composite~~ radar reflectivity measurements

58 such as the operational NWS Multi-Radar Multi-Sensor product (MRMS; Zhang et al., 2011;

59 Brodzik, 2022b). For example, Novak et al. (2006) defined a mesoscale band as having a length

60 > 250 km, width of 20 to 100 km, and radar reflectivity > 30 dBZ for at least 2 h. Numerical

61 weather prediction of p~~P~~recipitation rates within these potentially high-impact mesoscale bands

62 are challenging ~~to predict~~, in part because of the demonstrated variations in microphysical

63 properties and evolutionary processes, including rapid changes in crystal habits (Stark et al.,

64 2013) and degrees of riming (Colle et al., 2014) measured at the surface.

65   Mesoscale banding developed during a significant midlatitude cyclone on 4 February 2022

66 that produced widespread and diverse wintry-mixed precipitation spanning the midwest to

67 northeast U.S. At the surface, the cyclone was defined by a relatively weak, elongated low-

68 pressure center and stationary frontal boundary positioned along the U.S. northeastern coastline

69 (Zaremeba et al., 2024). As described in DeLaFrance et al. (2024b, see Fig. 2a and sec. 2.1), two

70   distinct regions of enhanced composite reflectivity developed northeast of the low-pressure

71   center. One of the regions of enhanced reflectivity was positioned on the warm side of the frontal

72   boundary and lacked well-defined banding structure but produced transitory mixed-phase wintry

73   precipitation including rain, ice pellets, and snow over the southern New England region and

74   extending offshore. A second region developed near the surface stationary front that extended

75   into New Hampshire and Maine and exhibited a well-defined banded structure, but with

76   decreasing composite reflectivity in time. Nonetheless, the reflectivity in this banded region was

77   consistently 6.5 to 9.0 dB greater than in the region that lacked well-defined banding. This

78   relative and persistent enhancement in reflectivity in the banded region despite its apparent decay

79   in time raises interesting questions about the evolutionary pathways for precipitating particles in

80   this region and their implications for surface precipitation.

81   Radar reflectivity measurements have a long history of use in estimating precipitation rates,

82   initially from simple empirically derived relationships between reflectivity and rain rate (e.g.,

83   Marshall and Palmer, 1948) and later extended to snowfall rates (e.g., Boucher and Wieler, 1985;

84   Fujiyoshi et al., 1990; Heymsfield et al., 2016). Ambiguity in precipitation intensity due to

85   varied microphysical particle properties has motivated the adoption of more complex

86   relationships derived from an improved understanding of the unique effects of microphysical

87   processes-based evolution on radar remote sensing measurements. Often these techniques are

88   derived from two or more coincident radar-based measurements (e.g., Grecu et al., 2016; Chase

89   et al., 2022; Dunnavan et al., 2023). Leveraging scattering dependencies based on the physical

90   properties of ice crystals and calculations based on modeled snowflakes of varied complexities

91   have shown promise in characterizing the unique effects of ice-phase microphysical processes

92   from coincident radar-based sources (e.g., Petty and Huang, 2010; Kneifel et al., 2011, 2015;

93   Leinonen and Moisseev, 2015; Leinonen and Szyrmer, 2015). Similarly, leveraging

94   dependencies of intrinsic particle fall velocity on their physical properties (e.g., Mitchell, 1996;

95   Heymsfield and Westbrook, 2010) and incorporating measurements from the radar Doppler

96   spectrum provides further constraint on process-based changes, especially during riming (e.g.,

97   Kalesse et al., 2016; Mason et al., 2018, 2019). Through development of novel methods to detect

98   and quantify the effects of microphysical processes from remote sensing radar measurements,

99   physical properties of the ice ~~natural~~ particles may be more accurately estimated. However, as

100   these retrieval techniques continue to become increasingly complex and adopt multi-source

101   measurements, validation of retrieved physical properties and inferred microphysical processes

102   using observations from ~~natural~~precipitating clouds remains crucially important.

103   Addressing this observational need, the Investigation of Microphysics and Precipitation for

104   Atlantic Coast-Threatening Snowstorms (IMPACTS) field campaign collected measurements

105   from ~~natural~~ precipitating clouds over the northeast and midwest U.S. during 36 science flights

106   over the 2020, 2022, and 2023 winters using a comprehensive suite of remote sensing and in situ

107   instruments (McMurdie et al., 2022a). Eleven science flights were conducted during the 2022

108   deployment with eight of those including coordination between the in situ cloud-sampling P-3

109   and overflying ER-2 aircraft providing coincident remote sensing and in situ measurements

110   within diverse winter storm environments (McMurdie et al., 2022b). These measurements have

111   direct application towards validating remote sensing retrieval of microphysical properties of ice

112   crystals (e.g., Chase et al., 2020, 2022; Matrosov et al., 2022; Finlon et al., 2022; Heymsfield et

113   al., 2023).

114   Elucidating process-based insights from temporally and spatially discontinuous airborne

115   measurements within an evolving and moving cloud system remains challenging. Numerical

116   modeling simulations are one method of connecting independent observations to microphysical

117   processes. However, bulk schemes require a limited representation of particle properties and

118   microphysical processes, thus presenting challenges for the integration of, or comparison with,

119   observations (Morrison et al., 2020). Moreover, three-dimensional dynamic simulations of winter

120   storms are subject to extrinsic uncertainties from design choices including initial conditions,

121   grid-cell resolution, and lead time (e.g., Colle et al., 2023). However, recent advances in

122   Lagrangian particle-based modeling techniques have shown promise in accurately simulating

123   ice-phase precipitation processes, typically at the expense of simplified dynamics and physical

124   domains (e.g., Jensen and Harrington, 2015; Brdar and Seifert, 2018; Bringi et al., 2020;

125   DeLaFrance et al., 2024a).

126   Recently, DeLaFrance et al. (2024b) used one-dimensional particle-based modeling

127   simulations constrained by IMPACTS observations to elucidate process-based insights on the

128   evolution of precipitating particles within the region of the 4 February 2022 winter storm that

129   lacked well-defined banding. Within this region of concurrent vapor deposition, efficient

130   aggregation, and riming, simulated particle evolution revealed that rime accumulations

131   accounted for a dominant 55% of the total ice-phase precipitation mass. Additionally, the riming

132   process produced a unique change in the vertical profile of Doppler velocity, consistent with the

133   coincident remote sensing radar observations. For this riming-dominant evolutionary pathway,

134   sensitivity simulations designed from observationally-informed perturbations of ambient

135   supercooled liquid water concentrations yielded a precipitation rate variability exceeding 60%

136   (DeLaFrance et al., 2024b). These perturbed states further demonstrated substantial variations in

137   reflectivity and Doppler velocity that emphasized differential effects of riming and aggregation

138   processes. These results warrant further investigation on the implications for the dependencies of

139   other ice-phase microphysical processes on their ambient environmental properties; in particular,

140   those associated with the banded region during this same event. With this motivation, this paper

141   aims to address four specific questions,

142

143   1. What was the microphysical evolutionary pathway of precipitating particles that

144   contributed to enhanced reflectivity along a mesoscale band during this IMPACTS winter

145   storm event?

146   2. What is the role of the ambient environment of the evolving particles in governing

147   precipitation fallout within the banded region?

148   3. What are the quantitative implications of sensitivities in the evolution of ice-phase

149   particles to their ambient environment properties?

150   4. To what extent are radar remote sensing measurements of reflectivity and Doppler

151   velocity modulated by process-based responses to perturbations in ambient

152   environmental properties?

153

154   To address these questions, we use numerical modeling simulations constrained by

155   IMPACTS observations from the banded region to assess process-based sensitivities and

156   quantify their imprint on radar remote sensing measurements. In the following section, we

157   introduce the IMPACTS instrumentation and observational strategy during the 4 February 2022

158   winter storm. Section 3 provides an observational analysis of the precipitation processes during

159   this event. In Section 4, we establish a control simulation and discuss its observational

160   validation. Section 5 describes four sensitivity simulations to assessing process-based

161 dependencies on the ambient environment. We provide some context for, and discuss the utility

162 of, our findings in Section 6 and offer concluding remarks in Section 7.

163

164
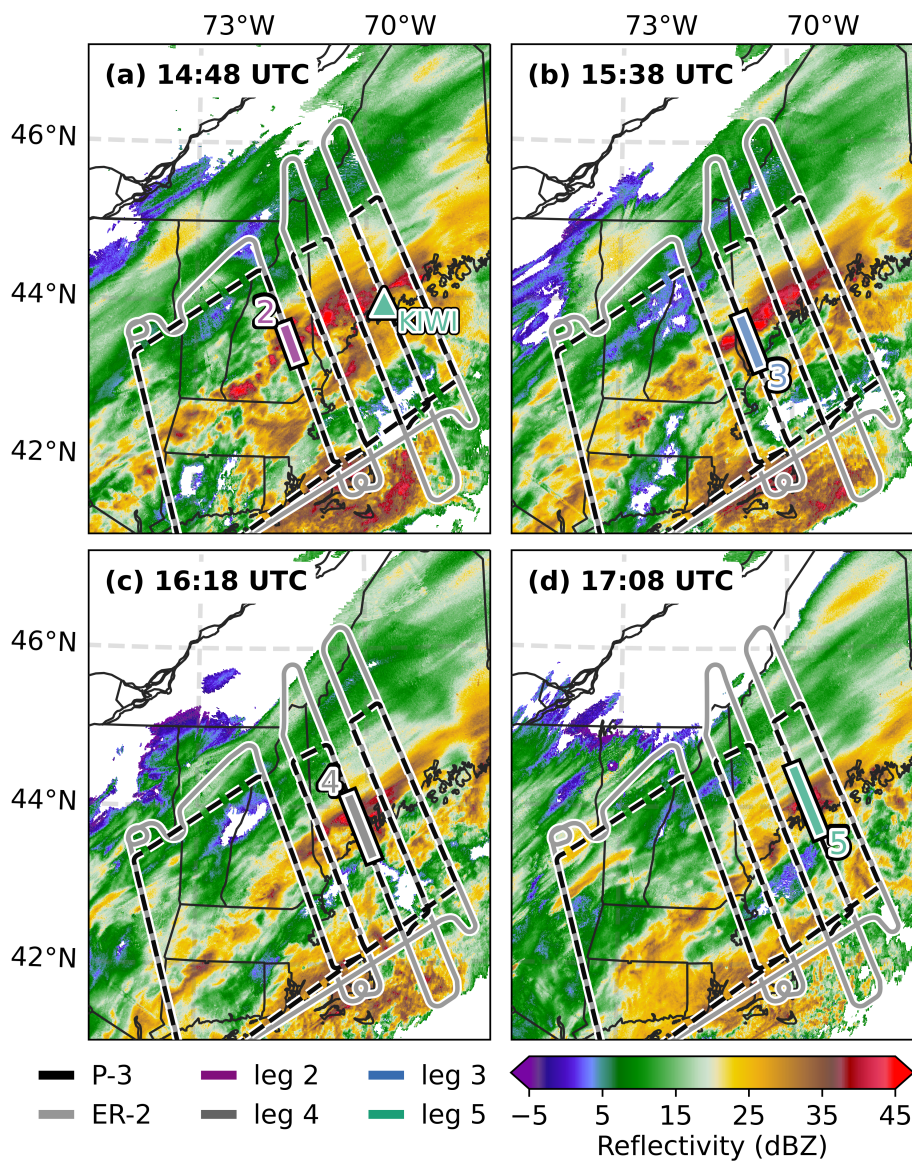
165 **Figure 1:** Flight tracks for the ER-2 and P-3 on 4 February 2022 and composite reflectivity
166 from the NWS MRMS product at the time of aircraft sampling within the region of analysis at
167 each flight leg as indicated by the colored lines. The ASOS surface locations for Portland, ME
168 (KPWM), Wiscasset, ME (KIWI) is , and Bangor, ME (KBGR) are shown in panel (a).

169

170 **2. Observations from a banded region of enhanced reflectivity during IMPACTS**

2.1. The 4 February 2022 winter storm

Because of the objective of IMPACTS to sample banded precipitation and that the colder region to the north and west of the surface front presented a greater likelihood of snowfall at the surface, a~~the~~ banded region near the front was the primary target of the 4 February science flights. Therefore, spatial and temporal coordination of sampling from the two IMPACTS aircraft was prioritized near the banded region. Composite radar reflectivity from the NWS MRMS product shown in Fig. 1 provides spatial and temporal context of the intended sampling objectives of IMPACTS flights relative to the prominent banded enhancement elongated southwest-to-northeast near the Gulf of Maine coastline. With passage of this band, steady ~~diverse~~ winter precipitation was~~characteristics were~~ reported at the Automated Surface Observing Stations (ASOS; Brodzik, 2022a) in Wiscasset, Maine (KIWI, location shown in Fig. 1a). Between 00:00 ~~UTC 4~~ and 07~~0~~:06~~0~~ UTC 4~~5~~ February, KIWI~~Portland, ME (KPWM; Fig. 1a)~~ reported ~~a mixture of rain,~~above freezing surface temperatures before rapidly decreasing below 0°C (Fig. 2a). ~~freezing rain, snow, and ice pellets~~ The hourly precipitation rate reached a modest maximum rate of 2.5 mm during the 12:00 UTC hour and precipitation intensity gradually reduced thereafter (Fig. 2b). A relative minimum in mean sea level pressure occurred at about 19:00 UTC 4 February (Fig. 2c), associated with the passage of the surface front~~while Bangor, ME (KBGR; Fig. 1a) experienced a transition from rain to snow by 01:25 UTC, which persisted through the duration of the storm. The Wiscasset, ME (KIWI; Fig. 1a) station reported a similar diversity in precipitation type as KPWM, with a modest peak hourly precipitation rate of 2.5 mm during the 12:00 UTC hour and a gradual reduction in intensity thereafter~~.

192
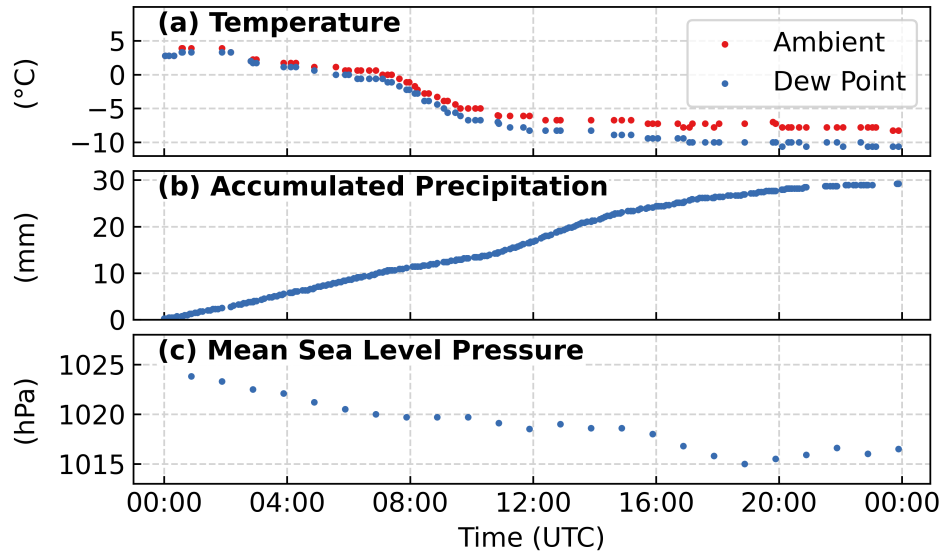
Figure 2: Time series of (a) ambient temperature and dew point, (b) accumulated precipitation, and (c) mean sea level pressure measurements on 4 February 2022 at the KIWI (Wiscasset, ME) ASOS site (indicated on Fig. 1).

IMPACTS executed a ~~semi-Lagrangian aircraft sampling~~ flight strategy consisting of six

flight legs in a "lawnmower-style" arrangement oriented orthogonal to the band that resulted in

semi-Lagrangian aircraft sampling from approximately 14:00 to 18:00 UTC (Fig. 1). In contrast

to sampling an evolving and moving storm along a flight leg fixed in space at varied altitudes

(i.e., Eulerian), an advantage of Lagrangian sampling is that it attempts to maintain temporal and

spatial continuity of the storm and the precipitating particles therein. Towards the objective of

Lagrangian sampling, the P-3 aircraft, equipped with in situ cloud probes, flew at a high altitude

initially and descended with each subsequent constant altitude leg, while horizontally translating

with the storm. The ER-2 was equipped with remote sensing instrumentation and flew in

coordination with the P-3 above the storm at constant altitude of approximately 20 km a.m.s.l.

To minimize temporal differences between the two aircraft owing to their differential air speeds,

each aircraft sampled the center points of the flight legs at nearly the same time and the center

points were positioned near the band's along-track composite reflectivity maxima.

210 On the initial flight leg, the P-3 sampled at a constant altitude of 6.2 km a.m.s.l. intersecting

211 the far western edge of the band. Flight leg 2, at an altitude of 5.5 km a.m.s.l., was positioned

212 northeast to better intersect the region of enhanced radar echo. The remaining legs were

213 positioned northeast of the previous leg at a distance that approximated the storm's advective

214 speed, each at a lower altitude and intersected the melting level on the final flight leg at 3.0 km

215 a.m.s.l. ~~This Lagrangian strategy requires that the storm maintain steady state during sampling.~~

216 ~~Thus, we suggest that flight legs 2 through 6 provided semi-Lagrangian context for coincident in~~

217 ~~situ and remote sensing measurements of the cloud and precipitation particles during evolution~~

218 ~~between 5.5 and 3.0 km a.m.s.l.~~ To constrain our analysis to the ice-phase precipitation processes

219 within this storm, in situ and remote sensing measurements from flight legs 2 through 5 (5.5 to

220 3.6 km a.m.s.l.) are used. Obtaining precise~~This~~ Lagrangian observations from temporally and

221 spatially evolving winter storms is exceptionally challenging and, from this strategy, requires

222 that the storm maintain steady state during sampling. However, m~~M~~easurements collected

223 between sampling along flight leg 2 (~14:45 UTC, Fig. 1a) and flight leg 5 (~17:15 UTC, Fig.

224 1d) occurred as the maximum composite reflectivity within the banded region weakened from

225 54.5 to 47.5 dBZ, which occurs at the radar bright band due to melting of the particles aloft. The

226 reduced intensity at the bright band suggests a change in the particle properties or the downward

227 mass flux from ice aloft, indicating~~ing~~ a decay of storm intensity, consistent with the reduction in

228 precipitation rate~~s~~ during the same time period. Thus, we suggest that flight legs 2 through 6

229 provided semi-Lagrangian context for coincident in situ and remote sensing measurements of the

230 cloud and precipitation particles during evolution between 5.5 and 3.0 km a.m.s.l.

231

232

233

2.2. IMPACTS observational assets

234   **2.2. IMPACTS observational assets**

235   The IMPACTS campaign benefited from a comprehensive suite of aircraft-based in situ and

236   remote sensing instrumentation onboard the cloud-penetrating P-3 and overflying ER-2 aircrafts.

237   From these instruments, the in situ measurements of precipitating particle properties and their

238   ambient environmental conditions coincident with remote sensing radar are crucial towards

239   addressing our research questions.

240   The P-3 aircraft was equipped with several particle probes to derive quantitative measures of

241   the physical properties and concentrations of ice- and liquid-phase populations of particles.

242   Measurements of the ice-phase particle size distributions (PSD) were derived from a vertically

243   oriented High-Volume Precipitation Spectrometer (HVPS) probe (Bansemer et al., 2022). The

244   HVPS is an Optical Array Probe (OAP), which permits sizing of a sampled ice crystal based on a

245   two-dimensional projected image (Lawson et al., 1993) from a 128-element array with a pixel

246   resolution of 150 μm (Bansemer et al., 2022). Thus, the HVPS is ideally suited to measuring

247   larger ice crystals, ~0.5 to 30.0 mm diameter. Commonly, the HVPS is paired with a Two-

248   Dimensional-Stereo (2D-S) OAP which also has a 128-element array but at a higher resolution of

249   10 μm and, therefore, is ideally suited for measuring small ice crystals. However, because the

250   2D-S did not operate during the 4 February flight, our analysis uses HVPS measurements to

251   derive in situ PSDs from ice crystals of diameters, D, > 0.5 mm. Measurements of the liquid-

252   phase particle population were derived from the Fast Cloud Droplet Probe (FCDP), a component

253   of the HAWKEYE combination probe, to estimate droplet sizes within a range of 2 to 50 μm

254   based on principles of Mie light scattering (Lawson et al., 2017). The National Center for

255   Atmospheric Research (NCAR) provided processing of the 1 Hz particle probe data (Bansemer

256   et al., 2022).

257   Particle imagery provides crucial evidence of the unique habits and geometric properties of

258   the ice crystals and permits inferences of the microphysical processes by which they evolved.

259   We use imagery collected from the Particle Habit Imaging and Polar Scattering Probe (PHIPS); a

260   novel instrument composed of two cameras separated by 120° with a resolution of 2 μm within a

261   field of view of approximately 3 x 2 mm (Schnaiter, 2022). For ambient environmental context,

262   in situ meteorological properties were measured by instrumentation onboard the P-3 aircraft to

263   derive pressure, temperature, dew point, and water vapor (Yang-Martin and Bennett, 2022).

264   Measurements of the three-dimensional ambient wind field were obtained from the Turbulent Air

265   Motion Measurement System (TAMMS; Thornhill, 2022). The TAMMS instrument is a system

266   of sensors distributed across the aircraft to estimate the horizontal and vertical components of the

267   winds and for configuration on the P-3 aircraft yields an estimated accuracy of 0.2 m s^{-1} for the

268   horizontal and vertical wind speeds (Thornhill et al., 2003; Thornhill, 2022). Supplementing the

269   IMPACTS airborne measurements, ambient meteorological conditions were obtained from

270   operational rawinsondes at NWS launch sites (Waldstreicher and Brodzik, 2022). Additionally,

271   standard NWS operational measurements including ASOS station data and composite radar from

272   the MRMS product were used to assess the surface conditions and provide large-scale context

273   during IMPACTS events.

274

275

276

277

278

279

280
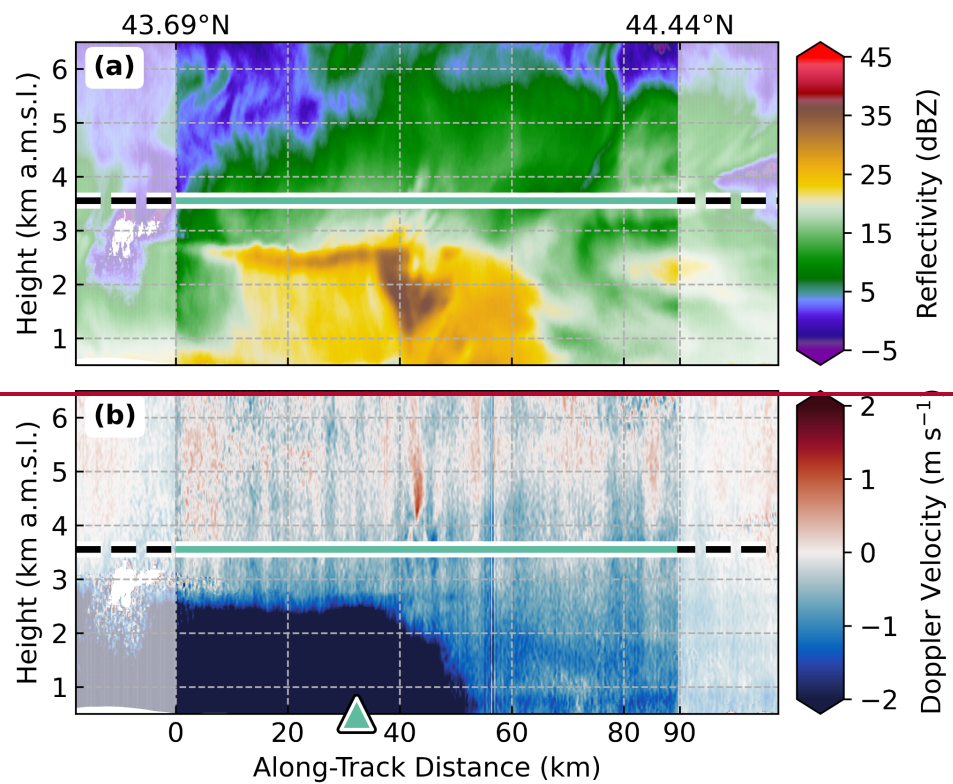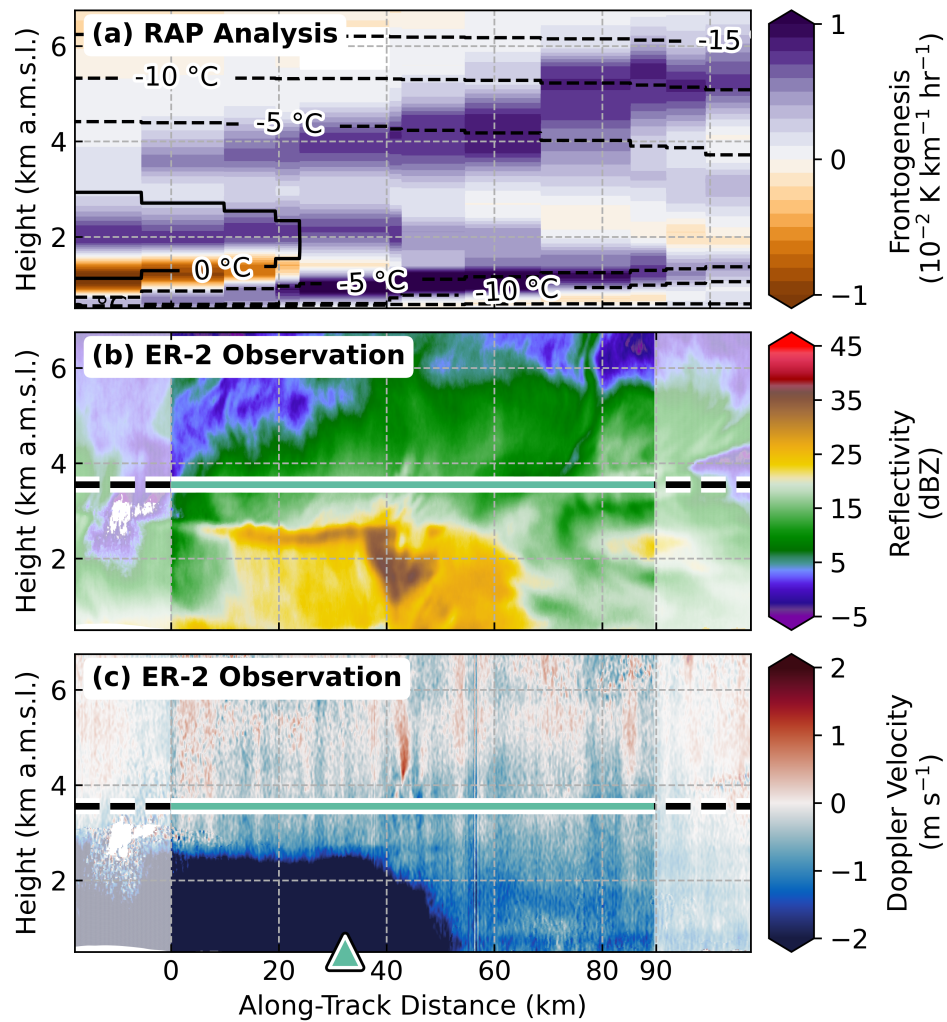
Figure ~~3~~2: Vertical cross sections of the (a)17:00 UTC RAP analysis frontogenesis and ambient air temperature (contoured) corresponding to the HIWRAP Ku-band radar (~~b~~a) reflectivity and (~~c~~b) Doppler velocity measurements from the ER-2 flight leg 5 as shown in Fig. 1d. Coincident sampling from the P-3 aircraft occurred at 3.6 km a.m.s.l. and the in situ observational extent assessed by frontal analysis is indicated by the horizontal green line spanning 43.69°N to 44.44°N. The marker in panel (~~c~~b) locates the KIWI (Wiscasset, ME) ASOS surface station positioned ~2.5 km west of the flight leg (see Fig. 1a).

The 4 February event was sampled by radar from the high-altitude ER-2 aircraft at Ku (13.9 Ghz), Ka (35.6 Ghz), and W bands (94 GHz). As an example of one flight leg, Fig. ~~3~~2 shows ~~the~~ vertical cross sections following the ER-2 on flight leg 5. Frontogenesis and ambient air

293 temperature derived from the 17:00 UTC NOAA Rapid Refresh (RAP) 13-km model (Benjamin

294 et al., 2016) is shown in Fig. 3a. Notably, there is a northward sloping frontal boundary aloft

295 indicated by the local maximum in ~~For~~frontogenesis. As the ER-2 as it overflew the frontal

296 band, radar reflectivity and Doppler velocity, ~~we use~~ measurements were collected from the

297 dual-band (Ku and Ka) High-Altitude Wind and Rain Airborne Profiler (HIWRAP; McLinden et

298 al., 2022), which has a vertical resolution of 150 m (Li et al., 2016). ~~As an example of one flight~~

299 ~~leg, Fig. 2 shows the vertical cross section of~~ Figure 3b-c shows these Ku-band reflectivity, Z_{Ku},

300 and Doppler velocity, V_{D_Ku} measurements, from the HIWRAP radar onboard the ER-2 ~~as it~~

301 ~~overflew the frontal band on flight leg 5~~ between ~17:08 and ~17:16 UTC. The P-3 aircraft

302 sampled this location at 3.6 km a.m.s.l. between ~17:05 and ~17:17 UTC. At the center point

303 over the band, the time difference between the two aircraft was 91 seconds. During flight leg 5,

304 the two aircraft overflew the KIWI ASOS station, which reported a precipitation rate of 1.02 mm

305 h^{-1} at its location ~2.5 km west of the flight leg (Fig. 1a) ~~and on the warm side of the frontal~~

306 ~~boundary~~. At KIWI, a radar bright band signature of the melting level occurs near 3 km a.m.s.l.

307 on the southern portion of the flight leg and abruptly terminates ~~The northward extent of the~~

308 ~~surface front is marked by the abrupt termination of the melting level~~ to the surface near 50 km

309 along-track distance. This termination of the melting level ~~which~~ is most apparent in the V_{D_Ku}

310 gradient (Fig. 3c~~2b~~) associated with the change in fall velocity of melting ice-phase particles.

311   The banded region was associated with a prominent cloud aloft, extending to about 6 km

312 a.m.s.l. Substantial decreases in Z_{Ku} were apparent immediately above a distinct vertical gradient

313 in Z_{Ku} at 6 km a.m.s.l. (Fig. 3b ~~2a~~). This vertical Z_{Ku} gradient exhibited small-scale [$O(1$ km)]

314 structural variabilities and filaments in Z_{Ku} down to the melting level. Similar small-scale [$O(1$

315 km)] structural variabilities were present in V_{D_Ku} near 6 km a.m.s.l., and within a background of

316   negative V_{D_Ku}, there were several isolated regions of substantial updrafts. Below 5 km a.m.s.l.,

317   V_{D_Ku} became increasingly negative, which indicated either increasing particle fall velocities or a

318   reduction in, or reversal of, ambient updrafts. The vertical cloud structure sampled by the ER-2

319   radar on flight leg 5 is suggestive of a weak generating cell layer near 6 km. a.m.s.l. and

320   precipitation fallstreaks (e.g., Rosenow et al., 2014; Plummer et al., 2014) towards the banded

321   region below. Operational rawinsondes launched at 12:00, 15:00, and 18:00 UTC from Portland,

322   Maine (KGYX), which was approximately overflown on flight leg 4, demonstrated a southwest

323   flow minimal directional wind shear above the frontal boundary (not shown). The lack of

324   directional wind shear aloft suggests that the primary transport of ice particles aloft occurred

325   within the vertical plane sampled by IMPACTS aircraft and minimally through horizontal

326   advection. Thus, we assume that successive collections of observations from descending P-3

327   flight legs cohesively translated with the storm motion and were minimally affected by

328   horizontal advection along sheared surfaces aloft.

329

330
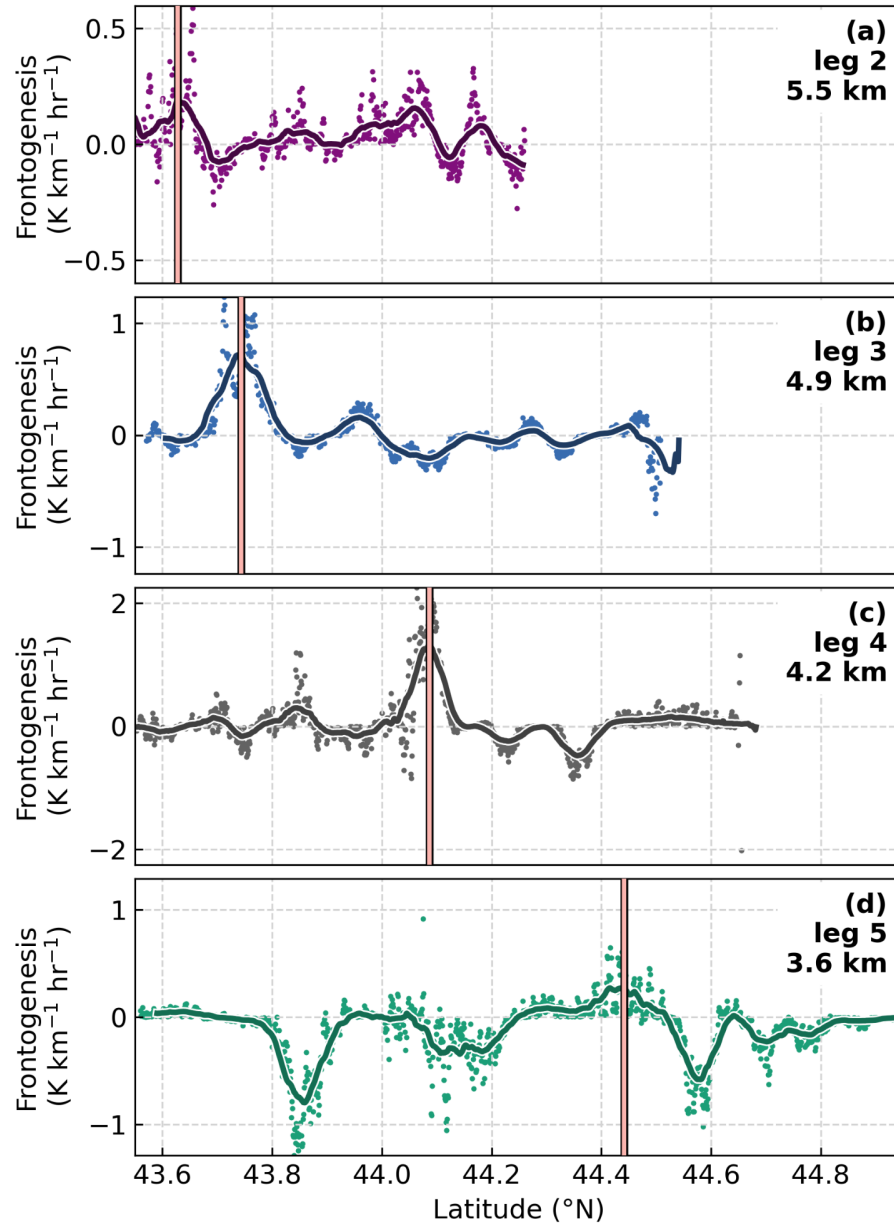
331   **Figure 43:** Frontogenesis computed from 1 Hz in situ measurements (dots) with smoothing
332 using a 60-s rolling mean (horizontal line) to estimate a maximum (vertical lines) along
333 individual P-3 flight legs 2 to 5. Mean altitudes of the P-3 are stated for each flight leg.
334

335

336

337

2.3. Observational context of in situ measurements

At either edge of the banded region, the horizontal extent of cloud aloft is marked by distinct gradients in Z_{Ku} (Fig. ~~3b~~2a). At the northern edge, a reduction in Z_{Ku} occurs at a region of significant shear in the precipitation fallstreaks, which is expected with a wind shift along a frontal boundary. Near this northern edge of the flight leg, a frontogenesis maximum is evident aloft in the RAP analysis (Fig. 3a). However, comparison of the RAP analysis (Fig. 3a) to prominent observed cloud characteristics including (i.e., melting level radar bright band and sloped frontal boundary, Fig. 3b-c) indicates some spatial or temporal uncertainty in the analysis. Therefore, we use the in situ environmental measurements to objectively identify the location of the frontal boundary, establishing flight-leg specific observational domains (i.e., observational regions indicated in Fig. 1 by different colors for each of the four flight legs) that preserve the intended Lagrangian in situ sampling of the evolving ice-phase particles.

To constrain our analysis to the air mass trailing the sloping front aloft, we define ~~The~~the northern extent of the horizontal observational domain ~~is identified~~ by a frontogenesis maximum. We compute frontogenesis from P-3 in situ measurements of horizontal winds, u and v, and potential temperature, θ, using the two-dimensional form of the (Miller, 1948) equation,

$$F_{2D} = \frac{1}{|\nabla\theta|}\left[-\frac{\partial\theta}{\partial x}\left(\frac{\partial u}{\partial x}\frac{\partial\theta}{\partial x} + \frac{\partial v}{\partial x}\frac{\partial\theta}{\partial y}\right) - \frac{\partial\theta}{\partial y}\left(\frac{\partial u}{\partial y}\frac{\partial\theta}{\partial x} + \frac{\partial v}{\partial y}\frac{\partial\theta}{\partial y}\right)\right].$$

Because of the considerable noise in frontogenesis computed from the 1Hz measurements, we apply a substantial smoothing using a 60-s rolling mean (Fig. ~~4~~3). We assess the northern extent of the observational domain for each flight leg by identifying a relative maximum in the smoothed frontogenesis. The frontogenesis analysis indicates a frontal boundary with an apparent northward gradient with increasing height, which primarily results from the southwest-

361 to-northeast orientation of the band. In addition, a northward sloping frontal boundary formed

362 from the warmer air mass to the south overrunning the cold surface air mass to the north.

363

flight leg	ER-2 start	ER-2 end	P-3 start	P-3 end
leg 2	14:50:46.5	14:54:16.0	14:48:35	14:54:17
leg 3	15:35:12.0	15:40:41.5	15:34:41	15:42:13
leg 4	16:17:47.0	16:24:40.5	16:11:25	16:23:23
leg 5	17:08:13.0	17:16:11.5	17:04:33	17:16:49

364 **Table 1**: Start and end times (UTC) of ER-2 and P-3 aircraft sampling on 4 February 2022
365 within the objectively identified observational domains for each flight leg, as indicated in Fig. 1.
366

367   At the southern edge of the band, there was a distinct absence of cloud during most of the

368 aircraft sampling along flight legs 2 through 5 (Fig. 1a-d). Thus, we assess the southern edges of

369 the observational domain at the altitude of the P-3 as the cloud edge. At each flight leg, we use

370 Z_{Ku} measurements at height of the P-3 aircraft to identify a reduction in Z_{Ku} below 0 dBZ. An

371 exception is made for flight leg 3, which intersected a transient cloud (Fig. 1b), where we instead

372 identify a relative minimum in Z_{Ku} (~5 dBZ). All further in situ observations used for analysis in

373 this study were obtained from within the complete segments spanning these flight-leg specific

374 cloud-edge-assessed southern points and the frontal-boundary-assessed northern points (Fig. 1).

375 Constrained by this approach, the evolutionary pathway of particles reaching the surface is

376 identified by observations of the particle properties and their ambient environment collected

377 within the cloud aloft at four altitudes descending in time. A summary of the start and end times

378 for ER-2 and P-3 flights along each flight leg traversing the objectively assessed, banded region

379 of cloud is provided in Table 1.

380
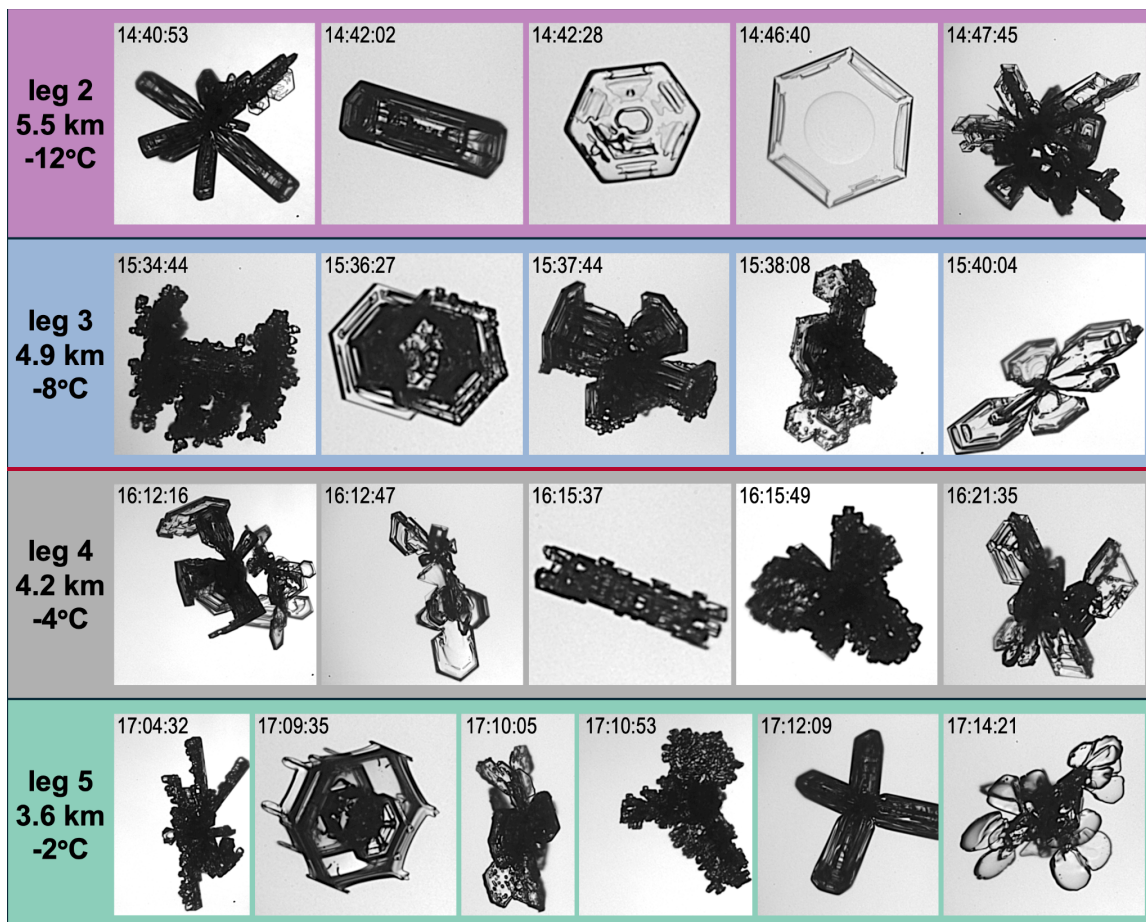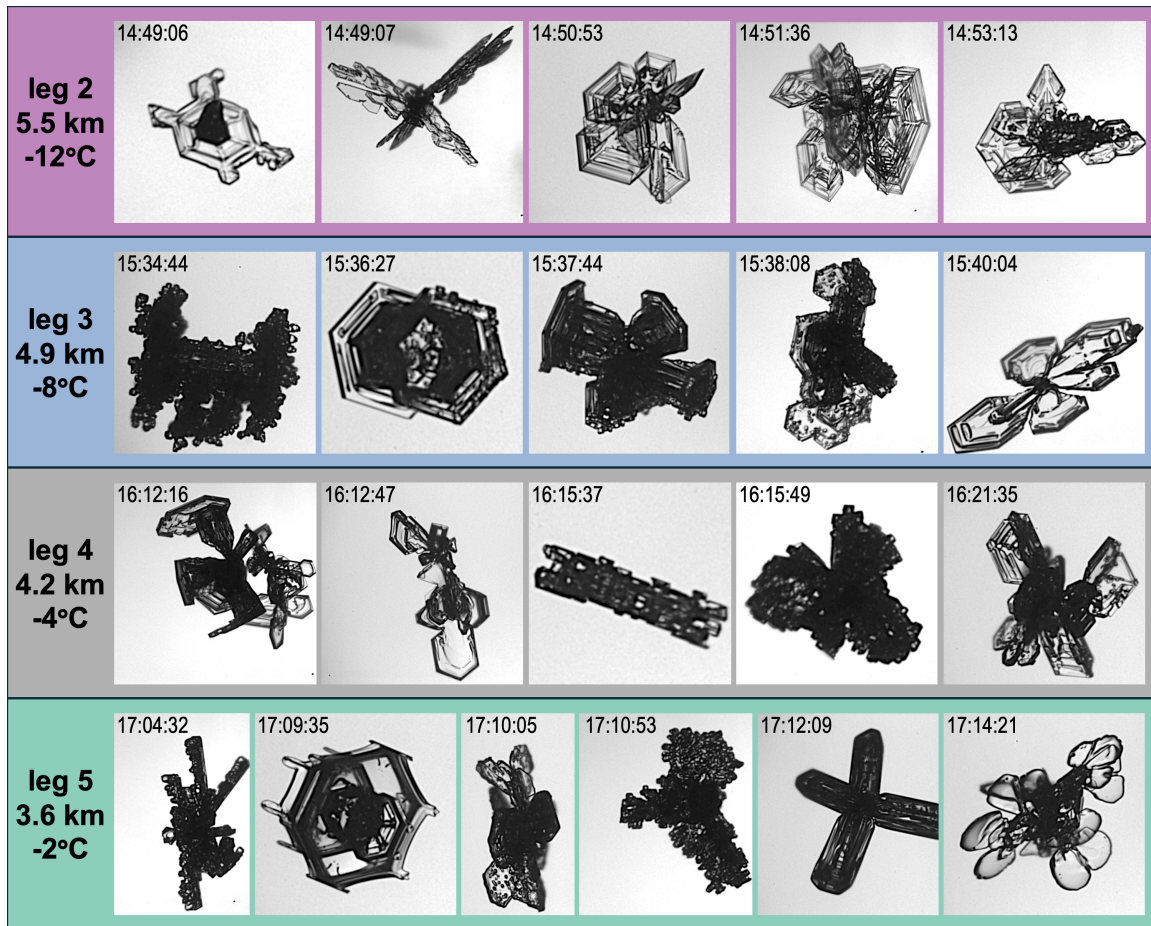
Figure 54: Particle imagery collected from the PHIPS probe within the banded regions of P-3 flight legs 2 to 5. Images are intended for representation of the crystal properties only and are not to scale. Mean altitudes of the P-3 and ambient temperatures are stated for each flight leg.

Particle imagery collected from the PHIPS probe on P-3 flight legs 2 through 5 are shown in Fig. 54. At 5.5 km a.m.s.l. and an ambient air temperature of -12°C, a ~~remarkable~~ diversity of crystal habits was observed including single crystal ~~columns (e.g., 14:42:02 UTC),~~ plates (e.g., 14:49~~2~~:06~~28 and 14:46:40~~ UTC), and dendrites (14:49:07 UTC) as well as polycrystalline structures of plates, dendrites, and sideplanes (e.g., 14:50~~47~~:03~~45, 14:51:36, and 14:53:13~~ UTC) ~~and bullet rosettes (e.g., 14:40:53 UTC)~~. Some of the particles at 5.5 km a.m.s.l. showed evidence of sublimation (e.g., 14:49~~2~~:06~~28~~ UTC) in the form of rounded corners and a smooth,

394 glossy appearance (Nelson, 1998). With descent on subsequent flight legs, there was increasing

395 evidence of sublimation. However, beginning at flight leg 3 at 4.9 km a.m.s.l. where the ambient

396 temperature was -8°C and relative humidity (RH) with respect to liquid water, 83%, there was

397 also evidence of riming with varied degrees of accumulated supercooled liquid water droplets

398 (e.g., 15:34:44 and 15:36:27 UTC). Similarly diverse crystal habits with varied degrees of rime

399 accumulation and sublimation were observed in imagery collected on flight leg 4 (4.2 km

400 a.m.s.l., -4°C, 82% RH) and flight leg 5 (3.6 km a.m.s.l., -2°C, 80% RH).

401 From PHIPS particle imagery collected at all heights, relative to the prevalence of single

402 crystals, very few aggregate particles were observed. However, transient occurrences of

403 aggregate particles were evident among HVPS images collected on flight legs 2 through 5 (not

404 shown). This near absence ofmodest evidence of aggregate particlesion significantly contrasts

405 withdiffers from the high prevalence of aggregate particles observed within the offshoresouthern

406 region of enhanced reflectivity that lacked well-defined banding (DeLaFrance et al., 2024b).

407 However, riming was evident in both regions. The presence of riming among particle

408 populations at flight legs 3 through 5 suggests a mixed-phase layer with an upper boundary

409 between 4.9 and 5.5 km a.m.s.l., but riming occurred heterogeneously throughout the mixed-

410 phase layer. Interestingly, populations of rimed particles were observed in close proximity to

411 sublimated particles (e.g., 15:38:08 and 15:40:04 UTC). Additionally, some particles appear to

412 have experienced riming followed by sublimation at some later time (e.g., 17:10:05 UTC),

413 whereas others appear to only experienced sublimation between formation aloft and 3.6 km

414 a.m.s.l. (e.g., 17:12:09 UTC). Collectively, particle imagery from above the band indicates a

415 dominant microphysical process between 5.5 and 3.6 km a.m.s.l. was sublimation. In Section 3,

416 we use in situ measurements to quantify the evolutionary effects of these observed microphysical

417 ~~processes on the ice-phase particles and provide environmental context through assessment of~~

418 ~~the ambient cloud properties.~~

419

420

421 **3. Properties of evolving ice-phase particles and their ambient environment**

422 Liquid-equivalent p~~P~~recipitation rates at the surface are governed by the particle mass and its

423 rate of fallout from cloud above. To determine the surface implications, we first quantify the

424 initial ice-phase precipitation mass aloft, at 5.5 km a.m.s.l., and its evolution within cloud

425 between 5.5 and 3.6 km a.m.s.l. Figure 6~~5~~ shows the median and interquartile range (IQR, 25th

426 and 75th percentile) ice mass PSDs from all HVPS measurements of particles with $D > 0.5$ mm

427 collected during~~from~~ P-3 flight legs 2 through 5. Consistent with DeLaFrance et al. (2024b), we

428 assume a mass–dimension relationship following Brown and Francis (1995). The greatest ice

429 mass concentration and largest particle sizes were identified at 5.5 km a.m.s.l. Additionally, we

430 found the most variability expressed by the IQR of PSDs at this height. However, based on the

431 observed diversity among crystal habits at 5.5 km a.m.s.l. (Fig. 5~~4~~), this variability in the

432 observed PSD is not surprising. ~~Although~~ Because measurements of ice at small particle sizes

433 are unavailable for the 4 February event, ~~particles larger than ~ 0.5 mm overwhelmingly~~

434 ~~dominate the contribution to~~ the total ice water content (IWC) is not completely defined by

435 measurements from~~and, thus,~~ the HVPS ~~measurements provide a valid estimate of the~~

436 ~~precipitation mass~~. Thus, throughout the present study, we define the characteristic IWC as the

437 fraction of IWC computed at $D > 0.5$ mm, applicable to both observations and models simulation

438 output. The median characteristic IWC at 5.5 km a.m.s.l. was 0.540 g m^{-3} and decreased to 0.278

439 g m^{-3} at 4.9 km a.m.s.l., then further decreased to 0.127 g m^{-3} at 4.2 km a.m.s.l. At 3.6 km

440 a.m.s.l., the characteristic IWC slightly increased to 0.148 g m⁻³; however, there was a notable

441 reduction of ice mass at the largest particle sizes, especially relative to 5.5 km a.m.s.l. (Fig. 6̶5̶a,

442 d).

443

444
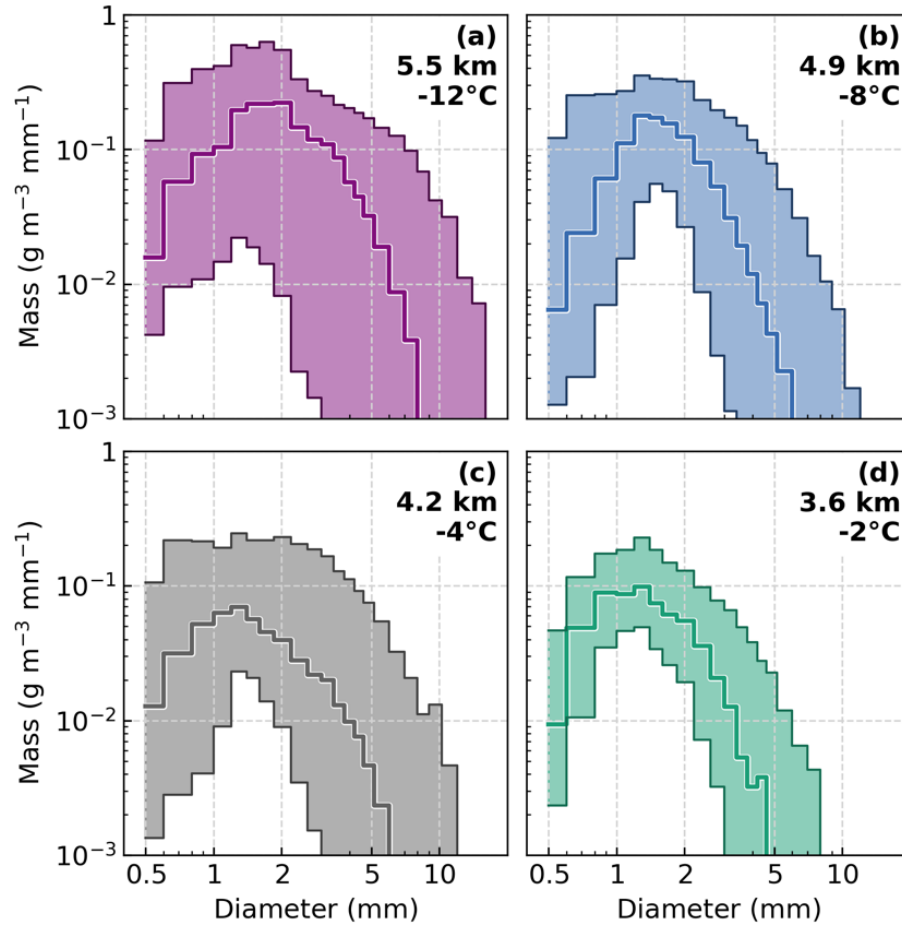
Figure 6̶5̶: Ice mass PSD median (line) and interquartile range (shaded) in situ measurements
from the HVPS probe at particle diameters > 0.5 mm within the banded regions of individual P-3
flight legs 2 to 5. Mean altitudes of the P-3 and ambient temperatures are stated for each flight
leg.

449

450   The relative maximum in ice mass at 5.5 km a.m.s.l. is consistent with the notion of ice-

451 phase particles concentrating aloft along the frontal boundary and maintained within a weak

452 generating cell layer (Fig. 3̶2̶). Precipitation fallout within the cloud below shows quantitative

453 evidence of sublimation in the characteristic IWC loss with descent, while a reduction in particle

454 size, especially among large particles, is consistent with the minimal evidence of aggregation in

455 the imaged particles (Fig. 54). The small increase in characteristic IWC between 4.2 and 3.6 km

456 a.m.s.l. occurs among particles ~0.5 to 2 mm in size and is most likely a result of accumulated

457 rime mass, despite the concurrent sublimation. Due to intermittency of the FCDP instrument on 4

458 February, measurements of the supercooled liquid water droplets population in the banded region

459 are available only for flight leg 5 at 3.6 km a.m.s.l. At this height, there was a mean liquid water

460 content (LWC) of 0.02 g m^{-3} and droplet diameter of 17 μm. However, imagery of supercooled

461 liquid droplets and rimed particles suggest that rime accumulation occurred at least as high as 4.9

462 km a.m.s.l (Fig. 54). The prominence of sublimation effects concurrent with riming presents a

463 distinctive evolutionary pathway for losses and accumulations of ice mass and requires a ~~unique~~

464 notable ambient environment supportive of these primary processes.

465

466
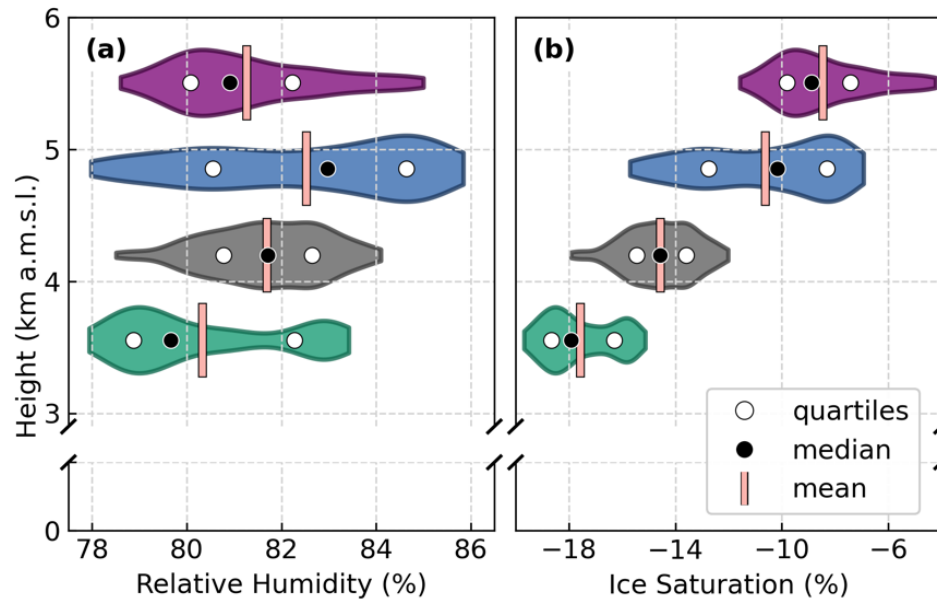
Figure 76: Violin plot distributions of (a) relative humidity and (b) ice supersaturation in situ measurements within the banded regions of flight legs 2 to 5. Outliers exceeding the 5th and 95th percentiles are not plotted.

Subsaturated conditions were found at all heights within the cloud. Figure 76a shows the measured ambient RH with respect to water at each P-3 flight level. The RH was similar through the vertical profile of cloud with median values from 79.7% (3.6 km a.m.s.l.) to 83.0% (4.9 km a.m.s.l.) and the range of variability was typically less than ~5-6% across each flight leg segment. Expressed as saturation with respect to ice in Fig. 76b, the cloud demonstrated an increasingly subsaturated ambient environment with descent. At 5.5. km a.m.s.l. (-12°C), the median ice saturation was -8.9% and further decreased to -17.9% at 3.6 km a.m.s.l. (-2°C). It is not readily apparent whether the magnitude of increasing subsaturation at lower heights (warmer temperatures) is representative of the cloud's ~~natural~~ vertical profile at any given time or a result of the temporal evolution between sampling at flight leg 2 and flight leg 5 (~2 h) within a decaying stage storm. Nonetheless, the subsaturated vertical profile is consistent with the evidence of sublimation among particle images at all heights (Fig. 54). However, riming requires the presence of supercooled liquid water droplets which, although are not sustained in a subsaturated environment, require time to evaporate. For example, within the median observed environmental conditions on flight leg 3 at 4.9 km a.m.s.l. (~83% RH, -8°C), droplets with an initial radius, r_0, of 10 μm will require ~10 s to evaporate and substantially longer for larger droplets (e.g., ~70 s for r_0 = 30 μm; Roy et al., 2023). It is plausible that s~~S~~upercooled liquid water droplets were ~~likely~~ formed in locally supersaturated environments outside of the observationally constrained domain of our analysis, ~~which occur within~~such as regions of sustained updrafts (e.g., Rauber and Tokay, 1991).

492
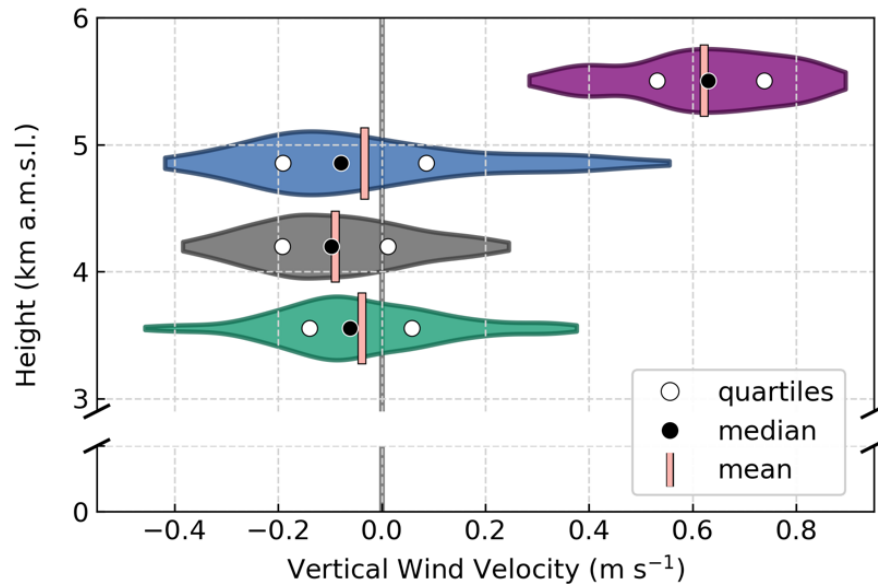
Figure 8~~7~~: Violin plot distributions of in situ measurements of vertical wind velocity from
the TAMMS instrument within the banded regions of P-3 flight legs 2 to 5. Outliers exceeding
the 5th and 95th percentiles are not plotted.

496

The distribution of ambient vertical wind velocity, w, measurements from the TAMMS

instrument on each P-3 flight leg are shown in Fig. 8~~7~~. Notably, there was a characteristic

ambient updraft at 5.5 km a.m.s.l. and abrupt transition to a weak downdraft below. This w

profile is consistent with the notion of a weak generating cell layer with precipitation fallout

inferred from the appearance along the prominent cloud top and fallstreaks in Z_{Ku} below ~5 km

a.m.s.l. from the radar cross section along flight leg 5 (Fig. 3b~~2a~~). At 5.5 km a.m.s.l., the median

w was 0.63 m s^{-1}, which is weaker than updrafts of 1 to 2 m s^{-1} that are common in generating

cells within winter cyclones (e.g., Rosenow et al., 2014; Kumjian et al., 2014; Keeler et al.,

2016). Between 4.9 and 3.6 km a.m.s.l., the ambient median wind field was characterized by

weak descent with w = ~ -0.06 to ~ -0.10 m s^{-1}, which is within the estimated uncertainty (of 0.2

m s^{-1}) of the TAMMS instrument. However, within this cloud layer, variabilities in w were

observed, and at all heights, updrafts were identified at the upper quartile of measurements. This

509   range of *w* variability was similarly evident in horizontal gradients of Doppler velocity across

510   flight leg 5, despite an overall descent below ~5 km a.m.s.l. (Fig. 3c2b). Intermittent updrafts

511   ~~appear to~~may have provided a source of supercooled liquid water within the subsaturated

512   ambient background environment. It is further plausible that supercooled liquid water transport

513   occurred through horizontal advection. However, because of the minimal evidence for

514   directional shear aloft, it appears more likely that supercooled liquid water transport, and more

515   importantly, particle evolution and fallout occurred within the vertical plane sampled by aircraft.

516   To support these observational inferences of microphysical processes associated with the band,

517   we use an observationally constrained numerical simulation and quantify the independent

518   process-based effects and their dependencies on properties of the ambient environment for

519   governing the cloud's precipitation mass and rate of fallout.

520

521   **4.   Control simulation design and validation**

522   Our modeling environment is designed to permit isolation and direct manipulation of

523   microphysical processes and the ambient environmental conditions to elucidate their independent

524   effects on an evolving ice-phase particle population. Model selection and its design follows

525   DeLaFrance et al. (2024b), which simulated the evolution of precipitating particles associated

526   with the southerly displaced region of enhanced reflectivity on 4 February. As in this prior study,

527   we use the Lagrangian particle-based McSnow model, which has a 1D columnar domain (Brdar

528   and Seifert, 2018). The McSnow model's particle-based scheme evolves an initial population of

529   ice-phase particles through explicit processes of deposition (sublimation), aggregation, and

530   riming within a prescriptive ambient environment. Constrained by the semi-Lagrangian in situ

531   and remote sensing measurements, this McSnow model permits simulations of the likely

532 evolution of a population of ice crystals. Furthermore, c̶C̶onsistent with the present study's

533 objectives, McSnow permits independent user control of these ice-phase processes, their regions

534 of activity or inactivity within the column, and properties of the ambient environment as

535 prescribed inputs. Furthermore, the ice-phase particle population evolves at the scale of the

536 particle, thereby removing assumptions about the evolving PSD, which is readily accessible

537 throughout the column. For comparability with simulations presented in DeLaFrance et al.

538 (2024b), we maintain consistency in the decisions regarding parameterizations and processing,

539 with select exceptions motivated by observed properties that were unique to each region of the

540 storm.

541   The first step is to create a control simulation that reproduces the observed evolution of

542 precipitating particles within their ̶n̶a̶t̶u̶r̶a̶l̶ ambient environment using inputs derived from in situ

543 measurements between P-3 flight legs 2 through 5. Particles are introduced in the model such

544 that the initial PSD at the upper boundary remains prescribed, which we derive from a Gamma

545 distribution fitted to the median PSD observed at 5.5 km a.m.s.l. at the uppermost P-3 flight leg

546 (Fig. 6̶5̶a). This initial PSD is represented̶c̶h̶a̶r̶a̶c̶t̶e̶r̶i̶z̶e̶d̶ by an estimated characteristic IWC of

547 0.540 g m^{-3} and total number concentration of 7 x 10^3 m^{-3} ($D > 0.225$ μm). Newly initiated

548 particles have a mass–dimension relationship of $m = 0.00294D^{1.94}$ (cgs) following Brown and

549 Francis (1995) for unrimed crystals but evolve independent of this assumption thereafter. Particle

550 terminal velocity, V_t, is derived following Heymsfield and Westbrook (2010). In McSnow,

551 modeled microphysical processes are largely independent of Eulerian grid constraints (see the

552 discussion in Brdar and Seifert, 2018, Sect. 2). However, a gridded columnar domain provides a

553 suitable framework for analysis of the evolved bulk particle properties. As in DeLaFrance et al.

554 (2024b), w̶W̶e specify a column of 500 grid cells, equating to a vertical resolution of 11 m, based

555   on an upper boundary at 5.5 km a.m.s.l. Particles evolve within a prescriptive ambient

556   environment, which is derived from the median value in situ measurements of standard

557   atmospheric properties (i.e., temperature, dew point, RH, pressure) at each flight altitude (Fig.

558   7~~6~~), and then linearly interpolating between measurements. Similarly, w is prescribed from linear

559   interpolation between median in situ measurements at each flight altitude (Fig. 8~~7~~).

560   The in situ observations of inferred microphysical processes motivated several design

561   considerations. Minimal evidence of aggregation throughout the column among particle imagery

562   (Fig. 5~~4~~) and an overall reduction in particle sizes with descent in cloud suggest a very low

563   process efficiency. With McSnow, upon collision, two particles will remain joined as an

564   aggregate particle dependent on a sticking efficiency parameter, E_{agg}, which scales from 0 to 1

565   (e.g., Pruppacher and Klett, 1997). Here, we adopt a sticking efficiency based on the laboratory

566   investigations of Connolly et al. (2012) in which they identify a maximum likelihood estimate

567   (MLE) and confidence interval (CI) for a temperature-dependent E_{agg}. Whereas in DeLaFrance et

568   al. (2024b) it was appropriate to adopt an E_{agg} following the upper range of the CI provided in

569   Connolly et al. (2012), here, we find it appropriate to adopt an E_{agg} following the lower range of

570   the CI. Therefore, E_{agg} has a value of 0.4 at -15°C and linearly reduces to 0 at -10°C, which is

571   maintained to 0°C. Because rimed particles were frequently observed in particle imagery at 4.9

572   km a.m.s.l., but not at 5.5. km a.m.s.l. (Fig. 5~~4~~), we define a mixed-phase layer of cloud below

573   5.0 km a.m.s.l. where riming occurs following a stochastic procedure (Brdar and Seifert, 2018)

574   based on prescriptive properties of the liquid water population. From the FCDP measurements,

575   we specify a LWC of 0.02 g m^{-3} and characteristic droplet radius of 8 μm. Consistent with

576   DeLaFrance et al. (2024b), all simulations run for 10 h at a time step of 5 s, and average the final

577   5 h, after reaching a steady state, for analysis.

578

579

580

581
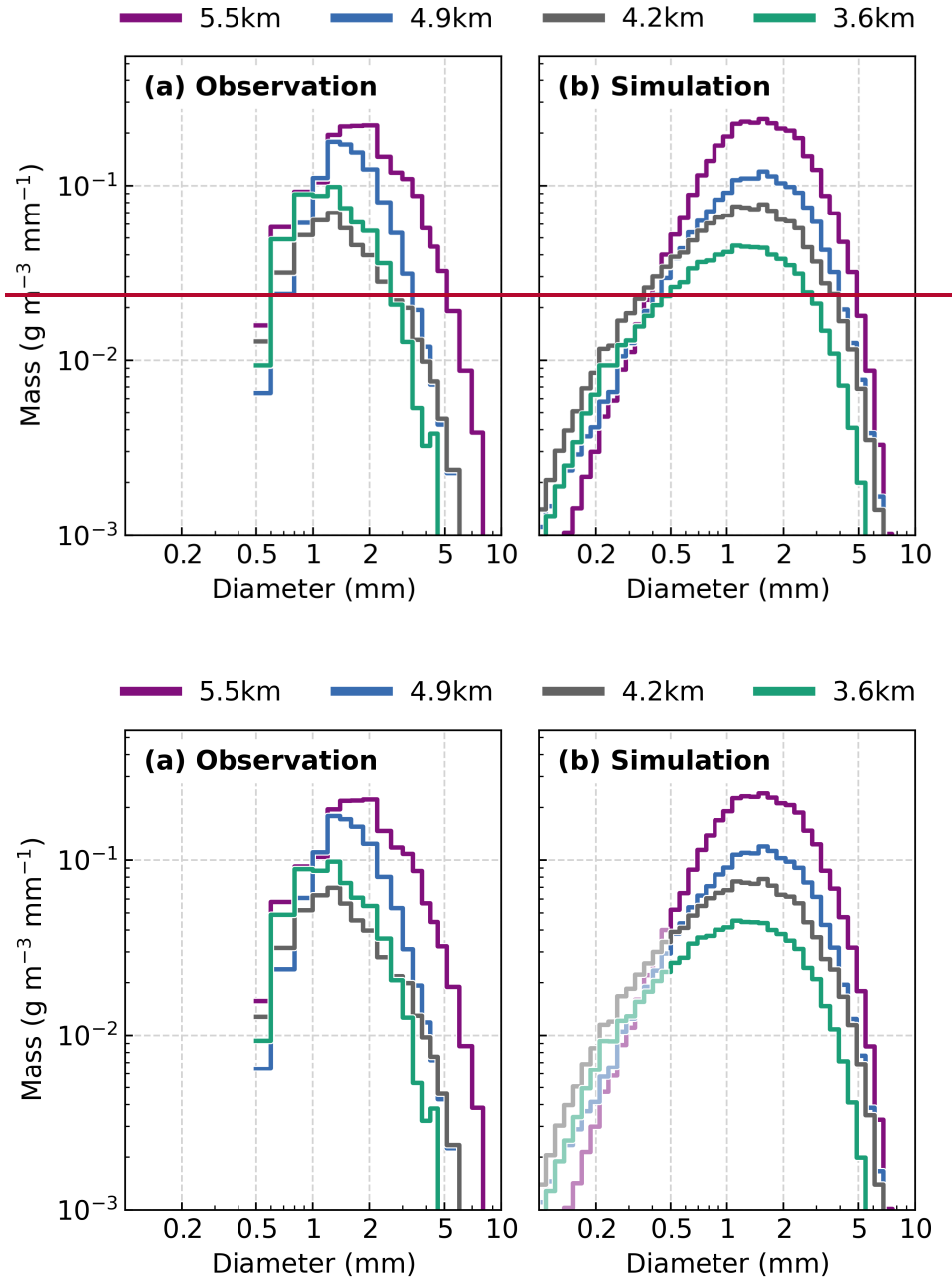
Figure 98: Composite ice mass PSDs from (a) in situ observations within banded regions of P-3 flight legs 2 to 5 (see Fig. 1a-d) and (b) the control model simulation at equivalent heights. For comparison purposes, line transparency of the simulations (b) is reduced at diameters less than 0.5 mm where observations are unavailable. Mean altitudes of the P-3 are stated for each flight leg.

587

588   To verify the control simulation, we first assess the evolution of the PSD throughout the ice-

589   phase layer of cloud. Specifically, we compare the model-simulated PSD with the median

590   observed PSD at each P-3 flight altitude. Figure 98a composites the flight-leg specific PSDs at D

591   > 0.5 mm, as shown in Fig. 65. The simulated PSD at equivalent heights from the model are

592   shown in Fig. 98b. A primary criterion towards establishing a successful control simulation was

593   a reproduction of the reduced characteristic IWC and particle sizes with descent that was

594   expressed in the observations. The control simulation has a vertical evolution of the PSD that

595   demonstrates consistency with observations, providing confidence that the modeled processes

596   are generally representative of the observednatural processes. At 5.5 km a.m.s.l., the control

597   simulation has an initial characteristic IWC of 0.606 g m^{-3}. Between 4.9, 4.2, and 3.6 km a.m.s.l.,

598   characteristic IWC decreased to 0.303, 0.214, and 0.119 g m^{-3}, respectively. Some of the unique

599   variabilities among the observations are not captured by the simulation. For example, the relative

600   increase in mass at $D = \sim 0.5$ to 2 mm between 4.2 and 3.6 km a.m.s.l. in observations (Fig. 98a)

601   is likely due to accumulation of rime mass. In the control simulation, the rime fraction, the

602   fractional mass attributable to accumulated rime, reaches 0.33 at 3.6 km a.m.s.l., which is

603   consistent with a subjective assessment of rime accumulation among the particle imagery at this

604   height (Fig. 54, leg 5). In the observed cloud, however, supercooled liquid water (and riming)

605   was heterogeneously distributed throughout the mixed-phase layer, which is not represented in

606   the model. While this limitation introduces some uncertainty in the simulated accumulation of

607   rime mass, the relatively small accumulated rime fraction of 0.33 is consistent with our

608   expectations based on prior simulations within the southerly displaced region of enhanced

609   reflectivity (DeLaFrance et al., 2024b). Within that region of the storm, there was an ~ 500 m

610   deeper mixed-phase layer and higher LWC of 0.05 g m⁻³, compared to 0.02 g m⁻³ within the

611   frontal region, and its similarly-constrained control simulation produced a rime fraction of 0.55.

612
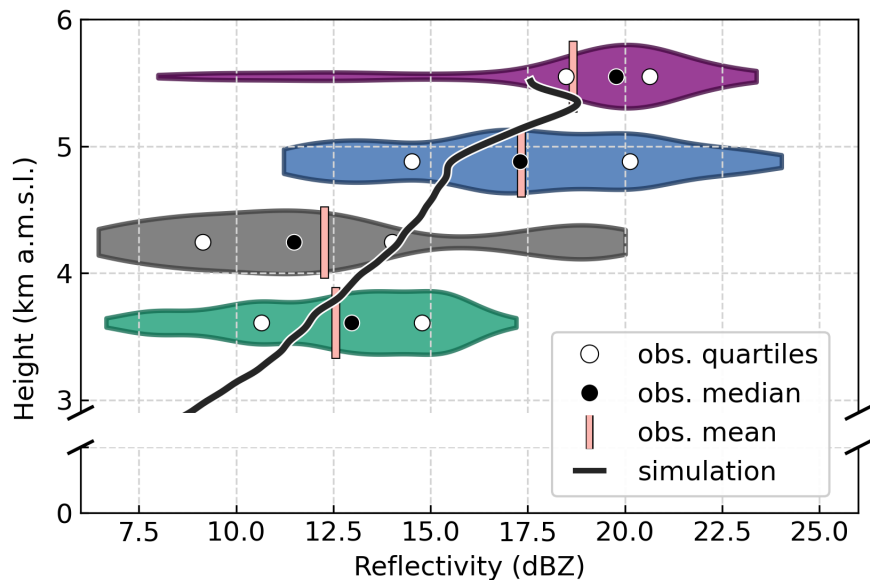
613   **Figure 109:** Ku-band radar reflectivity estimated from the control simulation and violin plot
614   distributions of reflectivity from the ER-2 HIWRAP Ku-band radar at the altitude of the P-3
615   aircraft within the banded regions of P-3 flight legs 2 to 5. Outliers exceeding the 5th and 95th
616   percentiles are not plotted.

617

618   Because we are motivated to identify the imprint of ice-phase microphysical processes and

619   their sensitivities to ambient conditions on radar remote sensing measurements, we further

620   evaluate the control simulation by computing Z_{Ku} from the evolved PSD, which is compared to

621   coincident measurements from the overflying ER-2 HIWRAP. Estimation of radar moments

622   from the simulated PSD follows DeLaFrance et al. (2024b) in applying a T-matrix approach

623   (Leinonen, 2014) to estimate the Ku-band radar backscatter cross section and a two-way path

624   integrated attenuation correction (Williams, 2022). Figure 109 shows the distribution of

625   HIWRAP Z_{Ku} measured at the height of the P-3 aircraft across each flight leg. The observed Z_{Ku}

626   maximized aloft and decreased between 5.5 and 4.2 km a.m.s.l., then slightly increased at 3.6 km

627   a.m.s.l. Throughout the cloud column, the control simulation demonstrates good agreement with

628   median observation values to within ~2-3 dB. The observed PSD and Z_{Ku} evolution with height

629   support a precipitation evolution pathway described by robust production or concentration of ice

630   within the updraft region of the generating cell layer along the frontal boundary aloft (~5.5 km

631   a.m.s.l.) and fallout within the downdraft regions below. This agreeing result establishes

632   confidence in the quasi-idealized 1D control simulation and, crucially, the simulated

633   microphysical processes within their ambient environment, prescriptively constrained by in situ

634   measurements.

635   Microphysical evolution between the generating cell layer at 5.5 km a.m.s.l. and 3.6 km

636   a.m.s.l. was dominated by sublimation, yielding a significant characteristic IWC loss. Riming,

637   whether within isolated regions of updrafts or following sublimation (i.e., Fig. 54, 17:10:05

638   UTC), negated some of the ice mass loss, as supported by the rime fractional mass of 0.33

639   accumulated at 3.6 km a.m.s.l. in the control simulation. Further, riming likely aided fallout

640   through increases in particle density, and subsequently fall speed. As a result, when assessed as

641   the vertical mass flux at 3.6 km a.m.s.l. (lowest altitude of P-3 observations), the control

642   simulation produced a liquid-equivalent rain rate of 0.66 mm h^{-1}. When compared toSurface

643   measurements at KIWI were, which reported as 1.02 mm during the 17:00 UTC hour, at the time

644   of aircraft overpass on flight leg 5 (Fig. 2), the control simulation appears to underestimate the

645   precipitation rate. However, the model does not account for liquid-phase precipitation which may

646   have formed below the melting level. Additionally, the surface precipitation rate at KIWI and

647   reduced to 0.76 mm h^{-1} during the following 18:00 UTC hour reduced to 0.76 mm h^{-1}., To the

648   extent that the control simulation precipitation rate can be compared to the available ASOS

649   tipping bucket measurements with a resolution of 0.254 mm, the simulation is in general

650 agreement with observations. Moreover, any underestimation of the precipitation rate by the

651 control simulation ~~in better agreement with the simulation.~~ may be a result, in part, of the

652 absence of simulated liquid-phase precipitation formation below the melting level. Despite the

653 subsaturated ambient environment, precipitation fallout was maintained through the cloud

654 contributing to a relative enhancement in surface precipitation rate with passage of the band.

655

656 **5. Ambient controls on particle evolution**

657 The frontal cloud exhibited a heterogeneity expressed in the diversity of ice crystal habits and

658 their apparent process-based evolution (e.g., sublimation and riming, Fig. 54) and similarly, in

659 the ambient RH (Fig. 76a) and the magnitude and direction of vertical winds below ~5 km

660 a.m.s.l. (Fig. 87). Despite the promising agreement between our control simulation and the

661 observations, a limiting assumption of the simulation is the reduction of the observed~~natural~~

662 cloud's heterogeneity to a prescriptive median state ambient environment. We are, therefore,

663 motivated to explore the particle evolution within perturbed ambient environments constrained

664 by the range of variability observed in the observed~~natural~~ cloud. In considering precipitation

665 pathways within these perturbed environments, we further aim to elucidate the ambient

666 dependencies of the dominant microphysical process and quantify those effects on surface

667 precipitation. Because the dominant microphysical processes acting on particles upon fallout

668 from the generating cell layer were sublimation and sedimentation, we perturb two properties of

669 the ambient environment that directly affect these processes and demonstrated a range of

670 variability in the ~~natural~~ cloud, RH and w (i.e., updrafts and downdrafts). From these ambient

671 properties, two groups of sensitivity simulations are designed from the interquartile ranges of in

672 situ measurements (Figs. 76a and 87).

673

674

675
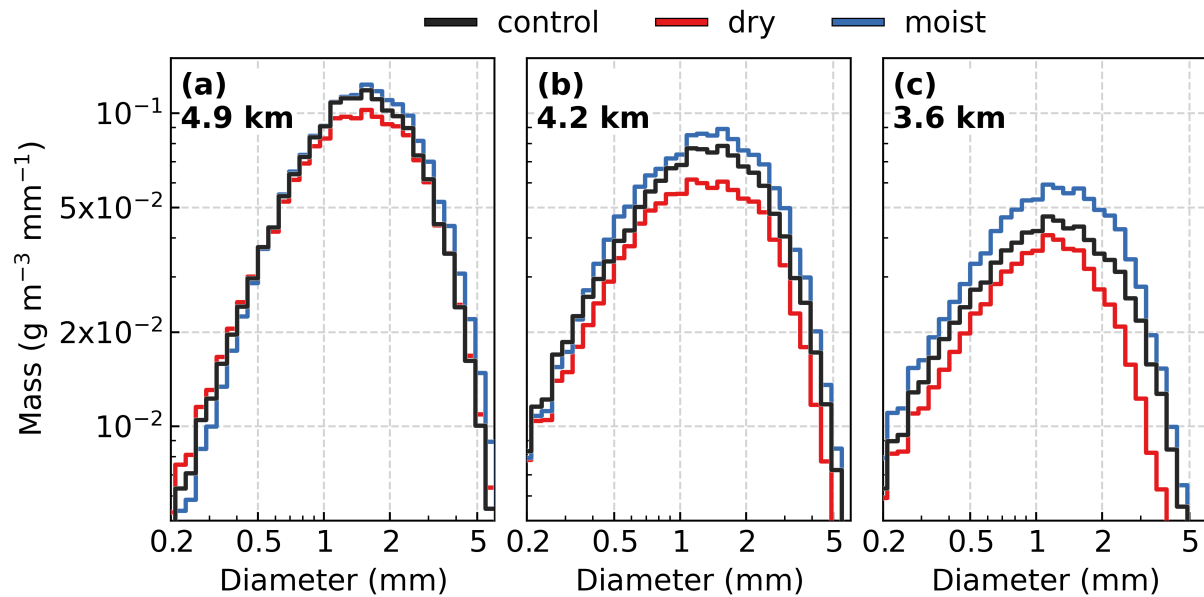
Figure 110: Ice mass PSDs for the control, dry, and moist simulations at (a) 4.9 km a.m.s.l. corresponding to P-3 flight leg 3, (b) 4.2 km a.m.s.l. corresponding to P-3 flight leg 4, and (c) 3.6 km a.m.s.l. corresponding to P-3 flight leg 5. Perturbed-state cloud RH profiles for the dry and moist simulations are derived from the interquartile range of in situ observations (see Fig. 76a).

680

5.1. Ambient relative humidity

For simulations which we term "dry" and "moist", the prescriptive cloud moisture input is

perturbed by assuming the 25th and 75th percentile values of observed RH (Fig. 76a). For both the

dry (25th percentile) and moist (75th percentile) simulations, most perturbations at all heights

were < 2% RH, with the largest perturbation being a decrease of 2.6% RH at 4.9 km a.m.s.l. in

the dry simulation and increase of 2.9% RH at 3.6 km a.m.s.l. in the moist simulation. Figure 110

shows the simulated PSD for the control, dry, and moist simulations. Although retrievable at any

height from the simulation, we found it convenient to assess the PSD at heights equivalent to P-3

flight legs 3 through 5. At 5.5 km a.m.s.l. (flight leg 2), where particles are initialized,

simulations do not meaningfully differ from each other. Between 4.9 and 3.6 km a.m.s.l. (Fig.

11<s>0</s>a-c), all simulations reproduce the reduction of the characteristic IWC with descent; however,

the extent of loss among all particle sizes is modulated by ambient RH. Table 2<s>1</s> quantitatively

summarizes the characteristic IWC at each height for the control and sensitivity simulations. At

3.6 km a.m.s.l., the characteristic IWC is further reduced from the control simulation by ~26% in

the dry simulation and increased by ~29% in the moist simulation. Because of the significant

effects of sublimational ice losses identified in the control simulation, it is perhaps unsurprising

that small perturbations (< ~2% RH) in the dry and moist simulation yield increasing departures

from the control with descent. Nonetheless, these simulations demonstrate a significant

dependency on ambient RH for the survival of ice mass falling through the ~2 km deep

subsaturated cloud layer.

height	observation	control	dry	moist	downdraft	updraft
5.5 km a.m.s.l.	0.540	0.606	0.600 [0%]	0.621 [+2.5%]	0.619 [+2.1%]	0.630 [+4.0%]
4.9 km a.m.s.l.	0.278	0.303	0.287 [-5.3%]	0.337 [+11.2%]	0.298 [-1.7%]	0.331 [+9.2%]
4.2 km a.m.s.l.	0.127	0.214	0.168 [-21.5%]	0.247 [+15.4%]	0.207 [-3.3%]	0.207 [-3.3%]
3.6 km a.m.s.l.	0.148	0.119	0.088 [-26.1%]	0.154 [+29.4%]	0.116 [-2.5%]	0.118 [-0.1%]

Table 2<s>1</s>: Simulated characteristic IWC (g m^{-3}) at heights equivalent to the P-3 aircraft on
flight legs 2 through 5 for the median observations and control, dry, moist, downdraft, and
updraft sensitivity simulations. Perturbed-state cloud RH profiles for the dry and moist
simulations are derived from the interquartile range of in situ observations (see Fig. 7<s>6</s>a).
Perturbed-state cloud vertical wind profiles for the downdraft and updraft simulations are derived
from the interquartile range of in situ observations (see Fig. 8<s>7</s>). Percentage differences in
characteristic IWC from the control simulation are provided for each perturbed-state simulation
in brackets.

713

714

715   **5.2. Ambient vertical wind magnitude and direction**

716   As with the ambient RH, we introduce two sensitivity simulations termed "downdraft" and

717   "updraft" which perturb the prescriptive ambient w by assuming the 25th and 75th percentile

718   values of observations (Fig. 8~~7~~). Perturbation at all heights for the downdraft (25th percentile)

719   simulation decreased w by ~0.1 m s^{-1}, yielding reduced updrafts in the generating cell layer and a

720   stronger downdraft below. Conversely, perturbations at all heights in the updraft (75th percentile)

721   simulation similarly increased w by ~0.1 m s^{-1}. This resulted in a completely ascending profile

722   throughout the cloud, albeit nearly static ($w = 0.01$ m s^{-1}) at 4.2 km a.m.s.l. Even in this

723   perturbed state at the upper quartile of observations, w in the generating cell layer is 0.74 m s^{-1},

724   whereas updrafts greater than ~1 m s^{-1} may be more typical of a generating cell layer. Thus,

725   given our observationally-constrained design specific to the 4 February event, our sensitivity

726   simulations assess a relatively small range of possible updraft and downdraft magnitudes within

727   generating cell clouds producing fallout precipitation.

728   Figure 12~~1~~ shows the evolved PSD for the control, downdraft, and updraft simulations.

729   Compared to RH, the evolved PSD demonstrates a reduced range of variation in response to the

730   w perturbations. Notably, the greatest differences between simulations manifest at small particle

731   sizes ($D < $ ~1 mm), which is a result of the differences in the particle's intrinsic V_t as the

732   particles reach 3.6 km a.m.s.l. (Fig. 12~~1~~c). In general, V_t increases with increasing particle size

733   (e.g., Locatelli and Hobbs, 1974). Thus, small particles have a relatively small intrinsic V_t and

734   when subject to a small perturbation in w (~0.1 m s^{-1}), experience an outsized net effect relative

735   to larger, faster falling particles. For example, at 3.6 km a.m.s.l. in the control simulation, 0.2

736   mm diameter particles attained a V_t of -0.42 m s^{-1}, whereas 2 mm particles had a V_t of -1.39 m s$^-$

737   ^{1}. Because ice mass is dominated by the larger, faster falling particles, which were minimally

738   affected by w perturbations, the characteristic IWC in the downdraft and updraft simulation at

739   3.6 km a.m.s.l. were strikingly similar to the control simulation (within 2.5%).

740

741

742
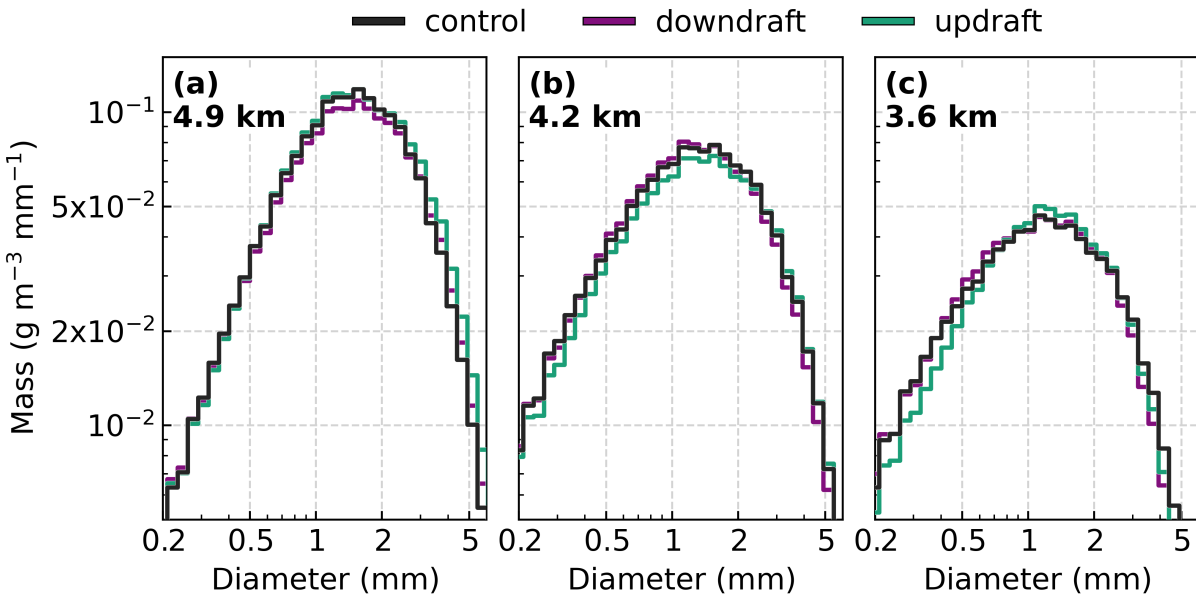
743   **Figure 12~~1~~:** Ice mass PSDs for the control, downdraft, and updraft simulations at (a) 4.9 km
744   a.m.s.l. corresponding to P-3 flight leg 3, (b) 4.2 km a.m.s.l. corresponding to P-3 flight leg 4,
745   and (c) 3.6 km a.m.s.l. corresponding to P-3 flight leg 5. Perturbed-state cloud vertical wind
746   profiles for the downdraft and updraft simulations are derived from the interquartile range of in
747   situ observations (see Fig. 8~~7~~).
748

749   The most notable influence of w on the characteristic IWC occurs in the updraft simulation at

750   4.9 km a.m.s.l (~9% increase, Table 2~~1~~). This local enhancement is likely due to the enhanced

751   lofting and concentrating of particles which must overcome a larger w in the updraft region

752   immediately above the 4.9 km a.m.s.l. evaluation height. However, any resultant enhancement in

753   the characteristic IWC from additional lofting within the updraft region appears to be negated

754   between 4.9 and 3.6 km a.m.s.l. by the outsized effect of sublimational ice loss among all particle

755   sizes. While the updraft within the generating cell layer is crucial to the production and

756   maintenance of a relatively high characteristic IWC aloft, perturbations of w in either the updraft

757   or downdraft regions yielded an inconsequential net effect on the characteristic IWC 3.6 km

758   a.m.s.l. However, the sedimentation rate of particles is modified by w perturbations. For

759   example, a 2 mm particle's sedimentation rate at 3.6 km a.m.s.l. in the downdraft simulation was

760   -1.52 m s^{-1}, whereas in the updraft simulation, the rate slowed to -1.36 m s^{-1}. The ice-phase

761   contribution to surface precipitation rates is governed by characteristic IWC, which has an

762   evolutionary sensitivity to ambient RH (Fig. 110), and its sedimentation rate, which is modified

763   by w. Because of the dependency on radar remote sensing measurements to estimate

764   precipitation rates and the diverse process-based outcomes from these ambient perturbations, we

765   next quantify these effects on vertical profiles of Z_{Ku} and V_{D_Ku}.

766

767
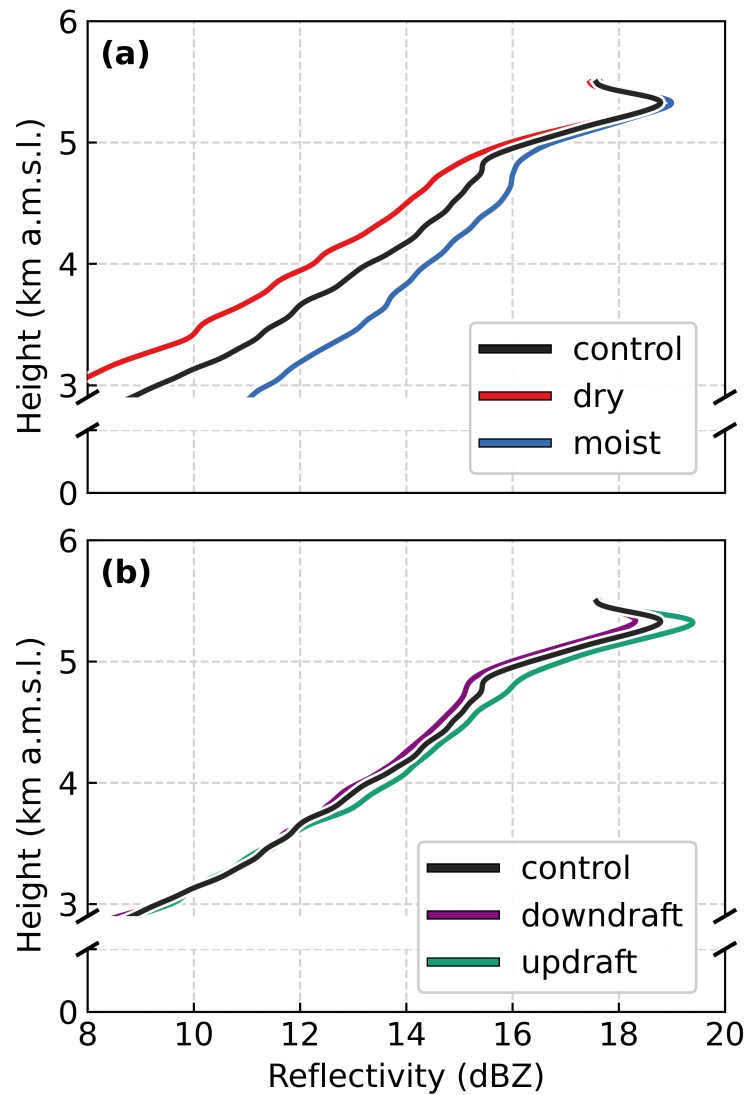
Figure 12: Ku-band radar reflectivity profiles for the (a) dry- and moist-perturbed and (b) updraft- and downdraft-perturbed sensitivity simulations relative to the control simulation.

5.3. Implications of process-based responses to ambient variabilities on radar remote sensing measurements

During the 4 February event, the enhancement in the composite reflectivity field along the band was a sustained, prominent feature that suggested a local enhancement in surface precipitation (Fig. 1). However, from vertical radar profiles across the band (e.g., Fig. 3), within

777   the ice layer there was a relative maximum in Z_{Ku} at the generating cell layer, which weakened

778   with descent in the fallout layer below. The more substantial maxima in column Z_{Ku} occurred

779   from melting near 3 km a.m.s.l. For the ice-phase precipitation aloft, this signature of Z_{Ku}

780   reduction with descent is a result of sublimational loss and an inefficient aggregation process,

781   which was supported by results of the control simulation. These losses through the cloud have

782   implications for the downward precipitation mass flux, and therefore, precipitation rates at the

783   surface. Thus, by quantifying the effects of process-based evolutionary responses to perturbed

784   ambient environments, we aim to determine the utility of remote sensing radar measurements to

785   discern ice-phase microphysical processes and their implications for precipitation mass and its

786   fallout.

787   Vertical profiles of Z_{Ku} estimated from the evolving PSD between 5.5 and 3 km a.m.s.l. are

788   shown in Fig. 1~~3~~2 for the control and sensitivity experiments. All simulations produce a relative

789   maximum in Z_{Ku} immediately below initialization at 5.5 km a.m.s.l. associated with the updraft

790   and concentration of ice mass followed by a continuous reduction in Z_{Ku} with descent thereafter,

791   which is consistent with the observations (Fig. 10~~9~~). A distinct change in the rate of change in

792   Z_{Ku} with height occurs at 5 km a.m.s.l. as a result of the initial onset of riming. Below 5 km

793   a.m.s.l., Z_{Ku} in the RH-perturbed environments becomes increasingly differentiated from the

794   control with descent (Fig. 1~~3~~2a). At 3.6 km a.m.s.l., Z_{Ku} was reduced in the dry simulation by 1.5

795   dB ~~(~12 %)~~ and increased in the moist simulation by 1.6 dB ~~(~13%)~~ relative to the control

796   (Table 3~~2~~). To provide context for these results, we estimate the liquid-equivalent precipitation

797   rate at 3.6 km a.m.s.l. Reducing RH by ~1 to 2% in the dry simulation yielded a precipitation

798   rate decrease of ~24%, whereas similarly increasing RH yielded a precipitation rate increase of

799   ~33% (Table 3~~2~~). Thus, modification of precipitation rate owed to differential ice losses by

800   sublimation as a result of perturbed RH below the generating cell layer has a direct implication

801   on the rate of change in Z_{Ku} with height. Perturbations in w produced a greater range of Z_{Ku}

802   variation aloft, within the updraft region, although, by 3.6 km a.m.s.l., the downdraft and updraft

803   simulations are nearly indistinguishable from the control (Fig. 132b). Similarly, the precipitation

804   rate at 3.6 km a.m.s.l. is not meaningfully affected by perturbation in w (Table 32).

805

806

height	property	control	dry	moist	downdraft	updraft
5.5 km a.m.s.l.	reflectivity (dBZ)	18.0	17.8 [-1.1%]	18.2 [+1.1%]	18.1 [+0.6%]	18.4 [+2.2%]
4.9 km a.m.s.l.	reflectivity (dBZ)	15.7	15.3 [-2.5%]	16.1 [+2.5%]	15.3 [-2.5%]	16.4 [+4.5%]
4.2 km a.m.s.l.	reflectivity (dBZ)	14.3	13.0 [-9.1%]	15.0 [+4.9%]	13.9 [-2.8%]	14.5 [+1.4%]
3.6 km a.m.s.l.	reflectivity (dBZ)	12.2	10.7 [-12.3%]	13.8 [+13.1%]	11.6 [-4.9%]	12.4 [+1.7%]
3.6 km a.m.s.l.	precipitation rate (mm h^{-1})	0.66	0.50 [-24.2%]	0.88 [+33.3%]	0.65 [-1.5%]	0.63 [-4.5%]

807

height	property	control	dry	moist	downdraft	updraft
5.5 km a.m.s.l.	reflectivity (dBZ)	18.0	17.8 [-0.2]	18.2 [+0.2]	18.1 [+0.1]	18.4 [+0.4]
4.9 km a.m.s.l.	reflectivity (dBZ)	15.7	15.3 [-0.4]	16.1 [+0.4]	15.3 [-0.4]	16.4 [+0.7]
4.2 km a.m.s.l.	reflectivity (dBZ)	14.3	13.0 [-1.3]	15.0 [+0.7]	13.9 [-0.4]	14.5 [+0.2]
3.6 km a.m.s.l.	reflectivity (dBZ)	12.2	10.7 [-1.5]	13.8 [+1.6]	11.6 [-0.6]	12.4 [+0.2]
3.6 km a.m.s.l.	precipitation rate (mm h^{-1})	0.66	0.50 [-24.2%]	0.88 [+33.3%]	0.65 [-1.5%]	0.63 [-4.5%]

808
809   **Table 32:** Simulated Ku-band radar reflectivity at heights equivalent to the P-3 aircraft on
810   flight legs 2 through 5 and liquid-equivalent precipitation rate at flight leg 5 for the control, dry,

811   moist, downdraft, and updraft sensitivity simulations. Perturbed-state cloud RH profiles for the
812   dry and moist simulations are derived from the interquartile range of in situ observations (see
813   Fig. 76a). Perturbed-state cloud vertical wind profiles for the downdraft and updraft simulations
814   are derived from the interquartile range of in situ observations (see Fig. 87). Magnitude
815   differences in reflectivity and precipitation rate from the control simulation are provided for each
816   perturbed-state simulation in brackets.
817

818   The insensitivity of precipitation rate to perturbations in w indicates that precipitation flux

819   through the subsaturated ice layer is more strongly governed by the characteristic IWC preserved

820   throughout the layer than by changes in the sedimentation rate of the ice particles. This principle

821   is similarly expressed by the simulated vertical profiles of V_{D_Ku} (Fig. 143). Whereas, relative to

822   the control simulation, perturbations in RH produced substantial differentiation in Z_{Ku} and,

823   ultimately, precipitation rate at 3.6 km a.m.s.l., a much smaller range of differentiation occurs for

824   V_{D_Ku} (Fig. 143a). At 3.6 km a.m.s.l., V_{D_Ku} in the dry and moist simulations are within 0.02 m s^{-1}

825   of the control simulation (-1.51 m s^{-1}). Similarly, while the updraft and downdraft simulations

826   appear to produce V_{D_Ku} profiles that are distinct from the control (Fig. 143b), the magnitude of

827   difference throughout the ice layer is explained by the magnitude of perturbation in w rather than

828   a change in the particles intrinsic V_t through perturbed microphysical evolution.

829

830

831

832
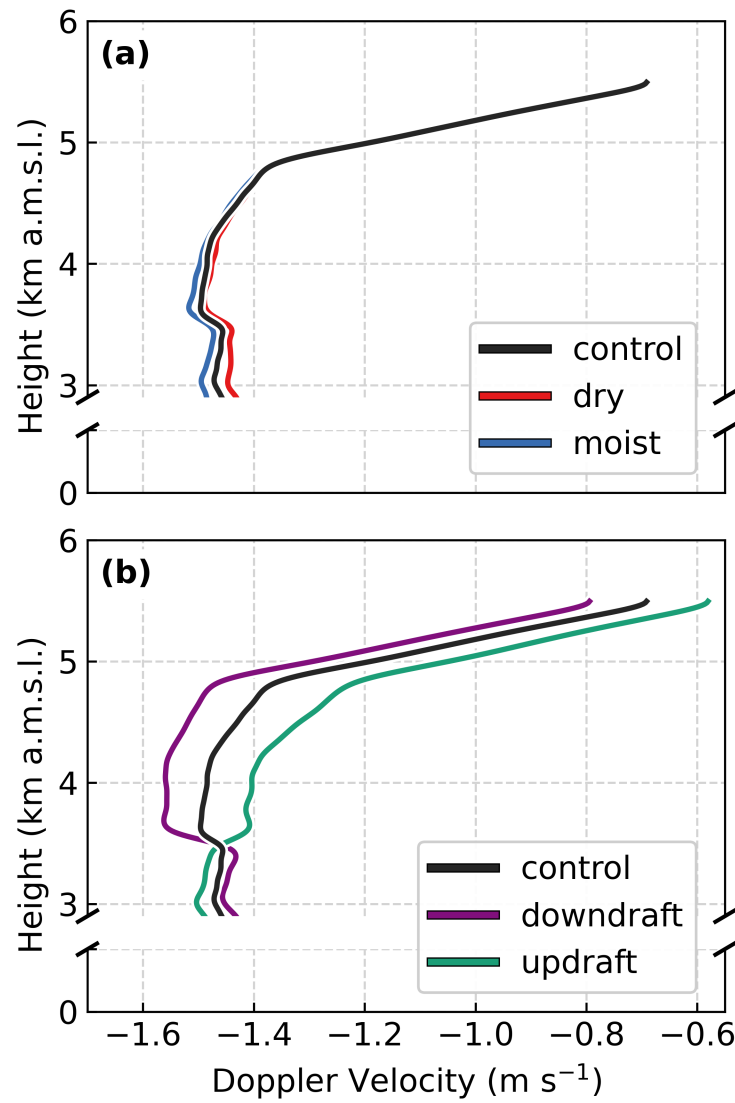
Figure 143: Radar Doppler velocity profiles for the (a) dry- and moist-perturbed and (b)
updraft- and downdraft-perturbed sensitivity simulations relative to the control simulation at Ku-
band.

6. Discussion

Despite the decaying stage of the winter storm, modest yet locally enhanced surface

precipitation rates (~1 mm h⁻¹) were sustained at the banded region by precipitation fallout from

the relatively high median characteristic IWC (0.540 g m⁻³) in the generating cell layer. Within

841   updraft regions of generating cell layers, airborne observations have revealed enhancements in

842   IWC (e.g., Houze et al., 1981; Plummer et al., 2015) and LWC (e.g., Wolde and Vali, 2001;

843   Evans et al., 2005; Ikeda et al., 2007; Plummer et al., 2014). These generating cell layers are

844   therefore a source region for significant precipitation enhancements in ambient environments

845   supportive of particle growth in the fallout region below. Indeed, prior studies have found that a

846   majority of IWC accumulation occurs below generating cell layers through vapor deposition and

847   aggregation (e.g., Herzegh and Hobbs, 1980; Plummer et al., 2015); two processes that were

848   notably absent in the fallout region of the banded cloud on 4 February. Thus, contrasting with the

849   precipitation pathways more commonly associated with generating cells, the dominant

850   microphysical process between the generating cell layer and the melting level was sublimation,

851   which yielded a substantial (> 70%) loss ~~of~~in the characteristic IWC.

852   The primary determinant for the rate of precipitation fallout from the banded cloud

853   contributing to surface enhancements was the amount of ice mass preserved through the

854   subsaturated layer. Sensitivity simulations demonstrated that, within this subsaturated

855   environment, particle evolution and its fallout have strong dependencies on the ambient RH (Fig.

856   11~~0~~) but weak dependencies on w (Fig. 12~~1~~) when independently assessed over an equivalent

857   range of observed variation. The intrinsic evolution of particle V_t during sublimation and,

858   subsequently, riming contributes an outsized effect on precipitation fallout relative to

859   perturbations of the ambient w, which affect the sedimentation rate. Nonetheless, the w profile

860   being characterized by a median state updraft in the generating cell layer and intermittent updraft

861   regions within overall descent below were necessary in establishing conditions favorable for the

862   riming that was observed in particle imagery. Although riming was not evident among particles

863   within the generating cell layer at 5.5 km a.m.s.l., rimed particles were prevalent at 4.9 km

864   a.m.s.l. and below, albeit heterogeneously distributed. Provided by a supply of supercooled

865   liquid water in updraft regions, riming is an efficient growth process for precipitation within and

866   below the generating cell (e.g., Houze et al., 1981; Plummer et al., 2014; Kumjian et al., 2014).

867   Rime accumulation appears to have had a prominent effect on the characteristic IWC. In the

868   control run simulation, approximately 33% of the characteristic IWC at 3.6 km a.m.s.l. was

869   attributable to rime accumulation. This contribution may even be underrepresented by the model

870   based on the smaller characteristic IWC in the simulation at 3.6 km a.m.s.l. and the increase in

871   characteristic IWC from 4.2 to 3.6 km a.m.s.l. in the observations which was not reproduced in

872   the simulation.

873   The resultant microphysical evolutionary pathways for particles within the banded region and

874   the southerly displaced region of enhanced reflectivity (Fig. 1) substantially differ. Riming was

875   prevalent in both regions, but to varied degrees. In the offshoresouthern region, DeLaFrance et

876   al. (2024b) identified robust particle growth by widespread riming which was enhanced by a

877   highly efficient, concurrent aggregation process. Consequently, despite a similar but reduced

878   magnitude of composite reflectivity (Fig. 1), simulated precipitation rates in the offshoresouthern

879   region were over two and a half times greater (1.77 mm h^{-1}) than those simulated for the banded

880   region (0.66 mm h^{-1}). These differences are demonstrative of the implications of process-based

881   modulation of microphysical properties, which remain challenging to constrain in remote sensing

882   retrievals, and underscores the need for ice-phase process discrimination in radar measurements.

883   In the present study, sensitivity simulations were used to quantify the imprint of sublimation

884   on vertical profiles of Z_{Ku} and V_{D_Ku}. We found that vertical profiles of Z_{Ku} demonstrate a

885   substantial sensitivity (~±1.512 to 13% dB) to varied rates of sublimational characteristic IWC

886   loss from perturbed RH environments (Fig. 132, Table 32) whereas V_{D_Ku} is relatively insensitive

887   to these perturbations (Fig. 1~~4~~3). Perturbations in w increase or decrease the magnitude of V_{D_Ku},

888   but the rate of V_{D_Ku} was dominated by the significantly greater median-state magnitude

889   differences between the updraft and downdraft regions. Whereas V_{D_Ku} was previously shown to

890   be especially sensitive to riming-based variabilities (DeLaFrance et al., 2024b), in the present

891   study, it provided no independent quantitative value towards differentiating effects of

892   sublimation (Fig. 1~~4~~3). Although not evaluated here, this finding likely extends to differentiation

893   of the effects of depositional growth, but for increasing Z_{Ku} with descent. In this scenario, an

894   equivalent sensitivity of Z_{Ku} but not V_{D_Ku} to depositional growth is analogous to the effects of

895   aggregation (DeLaFrance et al., 2024b). A similar ambiguity in the process-based distinction

896   between depositional growth and aggregation exists for multi-frequency radar techniques as

897   scattering models have shown dendritic and complex aggregation particles occupy a similar dual-

898   and triple-frequency radar scattering signatures (e.g., Petty and Huang, 2010; Kneifel et al.,

899   2011; Leinonen and Moisseev, 2015). Thus, discrimination between either low-density dendritic

900   or complex aggregate particle types or between deposition- or aggregation-dominant growth

901   from remote sensing measurements is likely to remain a challenge.

902

903   **7. Conclusions**

904   Mesoscale band development within winter storms is typically accompanied by

905   enhanced, and often, high-impact, surface precipitation rates over confined regions. The

906   microphysical properties of the ice-phase particles within these banded regions remain poorly

907   represented by numerical models and challenging to constrain in radar remote sensing retrievals,

908   owed in part to an incomplete understanding of the diverse microphysical pathways for banded

909   precipitation evolution. Addressing a need for more observations within ~~natural~~ clouds, the

910   IMPACTS campaign deployed a cloud-penetrating P-3 and overflying ER-2 aircraft to measure

911   properties of a mesoscale banded region of a northeastern U.S. winter storm on 4 February 2022.

912   During the ~3 h period that IMPACTS executed semi-Lagrangian sampling of the banded region,

913   the storm exhibited an apparent state of decay, weakening in composite radar reflectivity

914   intensity, yet maintaining a banded structure. This paper aimed to characterize the evolutionary

915   pathways for precipitation within the decaying-stage banded region, assess those implications for

916   surface precipitation, quantify sensitivities to ambient environmental properties, and determine

917   the imprint of microphysical process-based evolution on radar remote sensing measurements.

918   Surface precipitation along the band was associated with clouds that formed along a

919   stationary frontal boundary having a weak generating cell layer from ~6 to 5 km a.m.s.l. ($w =$

920   ~0.6 m s^{-1}) and precipitation fallstreaks between ~5 km a.m.s.l. and the melting level, near 3 km

921   a.m.s.l. The fallout region between the generating cell layer and melting level was characterized

922   by a weak downdraft ($w < \sim -0.1$ m s^{-1}) and subsaturated (RH = ~80 to 83%) ambient

923   environment. Particle imagery at all heights showed evidence of sublimation; however, riming

924   was also present in heterogeneously distributed regions of a mixed-phase layer extending to ~5

925   km a.m.s.l. We observed very little evidence of aggregation.

926   Quasi-idealized 1D model simulations using the Lagrangian particle-based McSnow

927   model were designed from observational constraints with prescriptive ambient environments.

928   The observed reduction in characteristic IWC, particle sizes, and Z_{Ku} with descent through the ~2

929   km deep fallout layer were reasonably reproduced by the control simulation and provided

930   confidence in the modeled representation of precipitating particle evolution within the

931   observednatural cloud. We designed four sensitivity simulations to elucidate evolutionary

932   dependencies on ambient cloud moisture and vertical air motions based on perturbations in the

933   prescribed RH and *w* profiles defined by the IQR of variability. From these sensitivity

934   simulations, we quantified sensitivities of particle growth and decay to ambient environmental

935   properties and estimated downward mass flux to determine the implications on precipitation

936   fallout within the banded region. Finally, these sensitivity simulations were used to determine the

937   process-based imprint on remote sensing measurements of Z_{Ku} and V_{D_Ku} within this unique

938   environment of the decay-state banded cloud. Collectively, the control simulation and four

939   sensitivity simulations have supported the following conclusions:

940

941   o   Enhanced surface precipitation rates during the passage of the mesoscale band resulted

942   from relatively high characteristic IWC formed within a generating cell layer that

943   produced ice-phase precipitation fallout within a descending layer below the generating

944   cells.

945   o   The ambient environment of the frontal cloud supported a dominant ice-phase

946   microphysical evolution by sublimation, and secondarily, riming processes to yield a net

947   characteristic IWC loss exceeding 70% within the subsaturated fallout layer.

948   o   Perturbations in ambient RH (~2%) yielded a substantial change in the characteristic

949   IWC preserved throughout the subsaturated layer (-26% to 29%) and in liquid-equivalent

950   precipitation rate (-24% to 33%); relative to RH, *w*-based perturbations (~0.1 m s^{-1})

951   yielded substantially decreased range of variability in characteristic IWC (< 2.5%) and

952   precipitation rate (< 4.5%).

953   o   Vertical profiles of Z_{Ku} were strongly dependent on RH-perturbed rates of sublimational

954   characteristic IWC loss throughout the cloud, but dependent on *w*-perturbed

955   sedimentation rates only in the updraft region; vertical profiles of V_{D_Ku} demonstrated

956   negligible microphysical process-based sensitivity.

957

958   The 4 February 2022 winter storm event provided a unique natural laboratory for assessing

959   process-based implications for ice-phase precipitation evolutionary pathways within winter

960   storms for several reasons. The winter storm was characterized by two distinct regions of

961   enhanced reflectivity with diverse surface precipitation rates owed to their unique microphysical

962   pathways. These regions were well sampled by aircraft during the IMPACTS field campaign,

963   providing crucial coincident in situ and remote sensing measurements with approximately

964   Lagrangian spatial and temporal context. The offshoresouthern region of enhanced reflectivity,

965   which lacked well-defined banding, experienced sustained particle growth above the melting

966   level dominated by riming (DeLaFrance et al., 2024b). The banded region to the north was more

967   strongly affected by the decaying stage of the storm from an intrusion of subsaturated air

968   throughout the ice-phase layer of cloud. Consequently, particle growth was unsupported by the

969   ambient environment of the banded region and ice loss through sublimation was a dominant

970   microphysical pathway. For each region, the storm's observed natural characteristics supported

971   the isolation of a microphysical process (i.e., riming or sublimation) in modeling sensitivity

972   simulations to assess their unique implications for surface precipitation and sensitivities to

973   ambient environmental properties. Results presented in the present study and DeLaFrance et al.

974   (2024b) provide new quantitative insights on the imprint of microphysical processes on radar

975   remote sensing measurements with application towards future retrieval algorithm development,

976   especially among those incorporating Doppler velocity measurements. Additionally, these

977   studies provide a framework of observational constraint and validation in future quasi-idealized

978 Lagrangian and particle-based modeling studies to further quantify the unique implications of

979 process-based microphysical evolution within diverse winter storm environments.

980

981

982 **Code and data availability**
983 IMPACTS data are publicly available through the NASA Distributed Active Archive Center
984 (https://doi.org/10.5067/IMPACTS/DATA101, McMurdie et al., 2019). Specific IMPACTS
985 datasets used for analysis include NCAR Particle Probes
986 (https://doi.org/10.5067/IMPACTS/PROBES/DATA101, Bansemer et al., 2022), Particle Habit
987 Imaging and Polar Scattering Probe (http://doi.org/10.5067/IMPACTS/PHIPS/DATA101,
988 Schnaiter, 2022), P-3 Meteorological and Navigation Data
989 (https://doi.org/10.5067/IMPACTS/P3/DATA101, Yang-Martin and Bennett, 2022), Automated
990 Surface Observing System (https://doi.org/10.5067/IMPACTS/ASOS/DATA101, Brodzik,
991 2022a), High Altitude Imaging Wind and Rain Airborne Profiler
992 (https://doi.org/10.5067/IMPACTS/HIWRAP/DATA101, McLinden et al., 2022), Turbulent Air
993 Motion Measurement System (https://doi.org/10.5067/IMPACTS/TAMMS/DATA101,
994 Thornhill, 2022), Multi-Radar/Multi-Sensor (MRMS) Precipitation Reanalysis for Satellite
995 Validation Product (https://doi.org/10.5067/IMPACTS/MRMS/DATA101, Brodzik, 2022b), and
996 NOAA Soundings (https://doi.org/10.5067/IMPACTS/SOUNDING/DATA201, Waldstreicher
997 and Brodzik, 2022).
998
999
1000
1001 **Author contributions**
1002 All authors contributed to decisions on methodologies applied throughout the study. AD
1003 performed the data analysis, modeling simulations, and processing of the model output. All the
1004 authors contributed to interpretations and assessed implications of the results. AD prepared the
1005 manuscript with contributions from all the co-authors.
1006
1007
1008 **Competing interests**
1009 The contact author has declared that none of the authors has any competing interests.
1010
1011

1012 **Acknowledgements**
1013 The authors acknowledge the IMPACTS team for their dedicated efforts in the collection and
1014 curation of the unique and exceptionally high-quality IMPACTS dataset. The authors also thank
1015 Aaron Bansemer for several helpful discussions regarding the interpretations and limitations of
1016 the processed microphysics probe data. Andrew DeLaFrance acknowledges NCAR for resources
1017 provided to visit its Mesoscale and Microscale Meteorology Laboratory (host Andrew J.
1018 Heymsfield), supporting the initial study conceptualization and design. We are grateful for the
1019 feedback received from three anonymous reviewers, which greatly improved this manuscript.

1020
1021
Financial support
This research was supported by the National Aeronautics and Space Administration (grant nos.
80NSSC21K1589, 80NSSC19K0338, and 80NSSC19K0397). Andrew J. Heymsfield is
supported by the National Science Foundation.

References
Bansemer, A., Delene, D., Heymsfield, A., and OBrien, J.: NCAR Particle Probes IMPACTS,
Dataset available online from the NASA Global Hydrometeorology Resource Center
DAAC, Huntsville, Alabama, USA [data set],
https://doi.org/10.5067/IMPACTS/PROBES/DATA101, 2022.
Benjamin, S. G., Weygandt, S. S., Brown, J. M., Hu, M., Alexander, C. R., Smirnova, T. G.,
Olson, J. B., James, E. P., Dowell, D. C., Grell, G. A., Lin, H., Peckham, S. E., Smith, T.
L., Moninger, W. R., Kenyon, J. S., and Manikin, G. S.: A North American Hourly
Assimilation and Model Forecast Cycle: The Rapid Refresh, Monthly Weather Review,
144, 1669–1694, https://doi.org/10.1175/MWR-D-15-0242.1, 2016.
Boucher, R. J. and Wieler, J. G.: Radar Determination of Snowfall Rate and Accumulation, J.
Appl. Meteorol. Clim., 24, 68–73, https://doi.org/10.1175/1520-
0450(1985)024<0068:RDOSRA>2.0.CO;2, 1985.
Bringi, V., Seifert, A., Wu, W., Thurai, M., Huang, G.-J., and Siewert, C.: Hurricane Dorian
Outer Rain Band Observations and 1D Particle Model Simulations: A Case Study,
Atmosphere, 11, 879, https://doi.org/10.3390/atmos11080879, 2020.
Brodzik, S.: Automated Surface Observing System (ASOS) IMPACTS, Dataset available online
from the NASA Global Hydrometeorology Resource Center DAAC, Huntsville,
Alabama, USA [data set], https://doi.org/10.5067/IMPACTS/ASOS/DATA101, 2022a.
Brodzik, S.: Multi-Radar/Multi-Sensor (MRMS) Precipitation Reanalysis for Satellite Validation
Product IMPACTS, Dataset available online from the NASA Global Hydrometeorology
Resource Center DAAC, Huntsville, Alabama, USA [data set],
https://doi.org/10.5067/IMPACTS/MRMS/DATA101, 2022b.
Brown, P. R. A. and Francis, P. N.: Improved Measurements of the Ice Water Content in Cirrus
Using a Total-Water Probe, J. Atmos. Ocean. Tech., 12, 410–414,
https://doi.org/10.1175/1520-0426(1995)012<0410:IMOTIW>2.0.CO;2, 1995.
Chase, R. J., Nesbitt, S. W., and McFarquhar, G. M.: Evaluation of the Microphysical
Assumptions within GPM-DPR Using Ground-Based Observations of Rain and Snow,
Atmosphere, 11, 619, https://doi.org/10.3390/atmos11060619, 2020.
Chase, R. J., Nesbitt, S. W., McFarquhar, G. M., Wood, N. B., and Heymsfield, G. M.: Direct
Comparisons between GPM-DPR and CloudSat Snowfall Retrievals, J. Appl. Meteor.
Clim., 61, 1257–1271, https://doi.org/10.1175/JAMC-D-21-0081.1, 2022.
Colle, B. A., Stark, D., and Yuter, S. E.: Surface Microphysical Observations within East Coast
Winter Storms on Long Island, New York, Mon. Weather Rev., 142, 3126–3146,
https://doi.org/10.1175/MWR-D-14-00035.1, 2014.
Colle, B. A., Yeh, P., Finlon, J. A., McMurdie, L., McDonald, V., and DeLaFrance, A.: An
Investigation of a Northeast U.S. Cyclone Event without Well-Defined Snow Banding
during IMPACTS, Mon. Weather Rev., 151, 2465–2484, https://doi.org/10.1175/MWR-
D-22-0296.1, 2023.

Connolly, P. J., Emersic, C., and Field, P. R.: A Laboratory Investigation into the Aggregation Efficiency of Small Ice Crystals, Atmos. Chem. Phys., 12, 2055–2076, https://doi.org/10.5194/acp-12-2055-2012, 2012.

DeLaFrance, A., McMurdie, L. A., Rowe, A. K., and Conrick, R.: Effects of Riming on Ice-Phase Precipitation Growth and Transport Over an Orographic Barrier, J. Adv. Model Earth Syst., 16, e2023MS003778, https://doi.org/10.1029/2023MS003778, 2024a

DeLaFrance, A., McMurdie, L. A., Rowe, A. K., and Heymsfield, A. J.: Simulated Particle Evolution Within a Winter Storm: Contributions of Riming to Radar Moments and Precipitation Fallout, Atmos. Chem. Phys., 24, 11191–11206, https://doi.org/10.5194/acp-24-11191-2024, 2024b.

Dunnavan, E. L., Carlin, J. T., Schvartzman, D., Ryzhkov, A. V., Bluestein, H., Emmerson, S., McFarquhar, G. M., Heymsfield, G. M., and Yorks, J.: High-Resolution Snowstorm Measurements and Retrievals Using Cross-Platform Multi-Frequency and Polarimetric Radars, Geophys. Res. Lett., 50, e2023GL103692, https://doi.org/10.1029/2023GL103692, 2023.

Evans, A. G., Locatelli, J. D., Stoelinga, M. T., and Hobbs, P. V.: The IMPROVE-1 Storm of 1–2 February 2001. Part II: Cloud Structures and the Growth of Precipitation, J. Atmos. Sci., 62, 3456–3473, https://doi.org/10.1175/JAS3547.1, 2005.

Finlon, J. A., McMurdie, L. A., and Chase, R. J.: Investigation of Microphysical Properties within Regions of Enhanced Dual-Frequency Ratio during the IMPACTS Field Campaign, J. Atmos. Sci., 79, 2773–2795, https://doi.org/10.1175/JAS-D-21-0311.1, 2022.

Fujiyoshi, Y., Endoh, T., Yamada, T., Tsuboki, K., Tachibana, Y., and Wakahama, G.: Determination of a $Z - R$ Relationship for Snowfall Using a Radar and High Sensitivity Snow Gauges, J. Appl. Meteorol., 29, 147–152, https://doi.org/10.1175/1520-0450(1990)029<0147:DOARFS>2.0.CO;2, 1990.

Ganetis, S. A., Colle, B. A., Yuter, S. E., and Hoban, N. P.: Environmental Conditions Associated with Observed Snowband Structures within Northeast U.S. Winter Storms, Mon. Weather Rev., 146, 3675–3690, https://doi.org/10.1175/MWR-D-18-0054.1, 2018.

Herzegh, P. H. and Hobbs, P. V.: The Mesoscale and Microscale Structure and Organization of Clouds and Precipitation in Midlatitude Cyclones. II: Warm-Frontal Clouds, J. Atmos. Sci., 37, 597–611, https://doi.org/10.1175/1520-0469(1980)037<0597:TMAMSA>2.0.CO;2, 1980.

Heymsfield, A., Bansemer, A., Heymsfield, G., Noone, D., Grecu, M., and Toohey, D.: Relationship of Multiwavelength Radar Measurements to Ice Microphysics from the IMPACTS Field Program, J. Appl. Meteorol. Clim., 62, 289–315, https://doi.org/10.1175/JAMC-D-22-0057.1, 2023.

Heymsfield, A. J. and Westbrook, C. D.: Advances in the Estimation of Ice Particle Fall Speeds Using Laboratory and Field Measurements, J. Atmos. Sci., 67, 2469–2482, https://doi.org/10.1175/2010JAS3379.1, 2010.

Heymsfield, A. J., Matrosov, S. Y., and Wood, N. B.: Toward Improving Ice Water Content and Snow-Rate Retrievals from Radars. Part I: X and W Bands, Emphasizing CloudSat, J.Appl. Meteorol. Clim., 55, 2063–2090, https://doi.org/10.1175/JAMC-D-15-0290.1, 2016.

Houze, R. A., Rutledge, S. A., Matejka, T. J., and Hobbs, P. V.: The Mesoscale and Microscale Structure and Organization of Clouds and Precipitation in Midlatitude Cyclones. III: Air

Motions and Precipitation Growth in a Warm-Frontal Rainband, J. Atmos. Sci., 38, 639–649, https://doi.org/10.1175/1520-0469(1981)038<0639:TMAMSA>2.0.CO;2, 1981.

Ikeda, K., Rasmussen, R. M., Hall, W. D., and Thompson, G.: Observations of Freezing Drizzle in Extratropical Cyclonic Storms during IMPROVE-2, J. Atmos. Sci., 64, 3016–3043, https://doi.org/10.1175/JAS3999.1, 2007.

Jensen, A. A. and Harrington, J. Y.: Modeling Ice Crystal Aspect Ratio Evolution during Riming: A Single-Particle Growth Model, J. Atmos. Sci., 72, 2569–2590, https://doi.org/10.1175/JAS-D-14-0297.1, 2015.

Kalesse, H., Szyrmer, W., Kneifel, S., Kollias, P., and Luke, E.: Fingerprints of a Riming Event On Cloud Radar Doppler Spectra: Observations and Modeling, Atmos. Chem. Phys., 16, 2997–3012, https://doi.org/10.5194/acp-16-2997-2016, 2016.

Keeler, J. M., Jewett, B. F., Rauber, R. M., McFarquhar, G. M., Rasmussen, R. M., Xue, L., Liu, C., and Thompson, G.: Dynamics of Cloud-Top Generating Cells in Winter Cyclones. Part I: Idealized Simulations in the Context of Field Observations, J. Atmos. Sci., 73, 1507–1527, https://doi.org/10.1175/JAS-D-15-0126.1, 2016.

Kneifel, S., Kulie, M. S., and Bennartz, R.: A Triple-Frequency Approach to Retrieve Microphysical Snowfall Parameters, J. Geophys. Res.-Atmos., 116, D11203, https://doi.org/10.1029/2010JD015430, 2011.

Kneifel, S., Von Lerber, A., Tiira, J., Moisseev, D., Kollias, P., and Leinonen, J.: Observed Relations Between Snowfall Microphysics and Triple-Frequency Radar Measurements, J. Geophys. Res.-Atmos., 120, 6034–6055, https://doi.org/10.1002/2015JD023156, 2015.

Lawson, P., Gurganus, C., Woods, S., and Bruintjes, R.: Aircraft Observations of Cumulus Microphysics Ranging from the Tropics to Midlatitudes: Implications for a "New" Secondary Ice Process, J. Atmos. Sci., 74, 2899–2920, https://doi.org/10.1175/JAS-D-17-0033.1, 2017.

Lawson, R. P., Stewart, R. E., Strapp, J. W., and Isaac, G. A.: Aircraft Observations of the Origin and Growth of Very Large Snowflakes, Geophys. Res. Lett., 20, 53–56, https://doi.org/10.1029/92GL02917, 1993.

Leinonen, J.: High-Level Interface to T-Matrix Scattering Calculations: Architecture, Capabilities and Limitations, Opt. Express, 22, 1655, https://doi.org/10.1364/OE.22.001655, 2014.

Leinonen, J. and Moisseev, D.: What do Triple-Frequency Radar Signatures Reveal about Aggregate Snowflakes?, J. Geophys. Res.-Atmos., 120, 229–239, https://doi.org/10.1002/2014JD022072, 2015.

Leinonen, J. and Szyrmer, W.: Radar Signatures of Snowflake Riming: A Modeling Study, Earth Space Sci., 2, 346–358, https://doi.org/10.1002/2015EA000102, 2015.

Li, L., Heymsfield, G., Carswell, J., Schaubert, D. H., McLinden, M. L., Creticos, J., Perrine, M., Coon, M., Cervantes, J. I., Vega, M., Guimond, S., Tian, L., and Emory, A.: The NASA High-Altitude Imaging Wind and Rain Airborne Profiler, IEEE T. Geosci. Remote, 54, 298–310, https://doi.org/10.1109/TGRS.2015.2456501, 2016.

Locatelli, J. D. and Hobbs, P. V.: Fall Speeds and Masses of Solid Precipitation Particles, J. Geophys. Res., 79, 2185–2197, https://doi.org/10.1029/JC079i015p02185, 1974.

Marshall, J. S. and Palmer, W. M. K.: The Distribution of Raindrops With Size, J. Meteorol., 5, 165–166, https://doi.org/10.1175/1520-0469(1948)005<0165:TDORWS>2.0.CO;2, 1948.

Mason, S. L., Chiu, C. J., Hogan, R. J., Moisseev, D., and Kneifel, S.: Retrievals of Riming and Snow Density from Vertically Pointing Doppler Radars, J. Geophys. Res.-Atmos., 123, 13807-13834, https://doi.org/10.1029/2018JD028603, 2018.

Mason, S. L., Hogan, R. J., Westbrook, C. D., Kneifel, S., Moisseev, D., and von Terzi, L.: The Importance of Particle Size Distribution and Internal Structure for Triple-Frequency Radar Retrievals of the Morphology of Snow, Atmos. Meas. Tech., 12, 4993–5018, https://doi.org/10.5194/amt-12-4993-2019, 2019.

Matrosov, S. Y., Korolev, A., Wolde, M., and Nguyen, C.: Sizing Ice Hydrometeor Populations Using the Dual-Wavelength Radar Ratio, Atmos. Meas. Tech., 15, 6373–6386, https://doi.org/10.5194/amt-15-6373-2022, 2022.

McLinden, M., Li, Lihua, and Heymsfield, Gerald M.: High Altitude Imaging Wind and Rain Airborne Profiler (HIWRAP) IMPACTS, Dataset available online from the NASA Global Hydrometeorology Resource Center DAAC, Huntsville, Alabama, USA [data set], https://doi.org/10.5067/IMPACTS/HIWRAP/DATA101, 2022.

McMurdie, L. A., Heymsfield, G., Yorks, J. E., and Braun, S. A.: Investigation of Microphysics and Precipitation for Atlantic Coast-Threatening Snowstorms (IMPACTS) Collection, Dataset available online from the NASA Global Hydrometeorology Resource Center DAAC, Huntsville, Alabama, USA [data set], https://doi.org/10.5067/IMPACTS/DATA101, 2019.

McMurdie, L. A., Heymsfield, G. M., Yorks, J. E., Braun, S. A., Skofronick-Jackson, G., Rauber, R. M., Yuter, S., Colle, B., McFarquhar, G. M., Poellot, M., Novak, D. R., Lang, T. J., Kroodsma, R., McLinden, M., Oue, M., Kollias, P., Kumjian, M. R., Greybush, S. J., Heymsfield, A. J., Finlon, J. A., McDonald, V. L., and Nicholls, S.: Chasing Snowstorms: The Investigation of Microphysics and Precipitation for Atlantic Coast-Threatening Snowstorms (IMPACTS) Campaign, B. Am. Meteorol. Soc., 103, E1243–E1269, https://doi.org/10.1175/BAMS-D-20-0246.1, 2022a.

McMurdie, L. A., Finlon, J. A., Heymsfield, G. M., and Yorks, J. E.: Investigation of Microphysics and Precipitation for Atlantic Coast Threatening Snowstorms (Impacts): The 2022 Deployment, in: IGARSS 2022 - 2022 IEEE International Geoscience and Remote Sensing Symposium, Kuala Lumpur, Malaysia, 4461–4464, https://doi.org/10.1109/IGARSS46834.2022.9883693, 2022b.

Miller, J. E.: On the Concept of Frontogenesis, J. Meteorol., 5, 169–171, https://doi.org/10.1175/1520-0469(1948)005<0169:OTCOF>2.0.CO;2, 1948.

Mitchell, D. L.: Use of Mass- and Area-Dimensional Power Laws for Determining Precipitation Particle Terminal Velocities, J. Atmos. Sci., 53, 1710–1723, https://doi.org/10.1175/1520-0469(1996)053<1710:UOMAAD>2.0.CO;2, 1996.

Morrison, H., Van Lier-Walqui, M., Fridlind, A. M., Grabowski, W. W., Harrington, J. Y., Hoose, C., Korolev, A., Kumjian, M. R., Milbrandt, J. A., Pawlowska, H., Posselt, D. J., Prat, O. P., Reimel, K. J., Shima, S., Van Diedenhoven, B., and Xue, L.: Confronting the Challenge of Modeling Cloud and Precipitation Microphysics, J. Adv. Model Earth Syst., 12, e2019MS001689, https://doi.org/10.1029/2019MS001689, 2020.

Nelson, J.: Sublimation of Ice Crystals, J. Atmos. Sci., 55, 910–919, https://doi.org/10.1175/1520-0469(1998)055<0910:SOIC>2.0.CO;2, 1998.

Novak, D. R., Bosart, L. F., Keyser, D., and Waldstreicher, J. S.: An Observational Study of Cold Season–Banded Precipitation in Northeast U.S. Cyclones, Weather Forecast., 19, 993–1010, https://doi.org/10.1175/815.1, 2004.

1202 Novak, D. R., Waldstreicher, J. S., Keyser, D., and Bosart, L. F.: A Forecast Strategy for
1203   Anticipating Cold Season Mesoscale Band Formation within Eastern U.S. Cyclones,
1204   Weather Forecast., 21, 3–23, https://doi.org/10.1175/WAF907.1, 2006.
1205 Novak, D. R., Colle, B. A., and Yuter, S. E.: High-Resolution Observations and Model
1206   Simulations of the Life Cycle of an Intense Mesoscale Snowband over the Northeastern
1207   United States, M. Weather Rev., 136, 1433–1456,
1208   https://doi.org/10.1175/2007MWR2233.1, 2008.
1209 Petty, G. W. and Huang, W.: Microwave Backscatter and Extinction by Soft Ice Spheres and
1210   Complex Snow Aggregates, J.Atmos. Sci., 67, 769–787,
1211   https://doi.org/10.1175/2009JAS3146.1, 2010.
1212 Plummer, D. M., McFarquhar, G. M., Rauber, R. M., Jewett, B. F., and Leon, D. C.: Structure
1213   and Statistical Analysis of the Microphysical Properties of Generating Cells in the
1214   Comma Head Region of Continental Winter Cyclones, J. Atmos. Sci., 71, 4181–4203,
1215   https://doi.org/10.1175/JAS-D-14-0100.1, 2014.
1216 Pruppacher, H. R. and Klett, J. D.: Microphysics Of Clouds And Precipitation, 2nd rev. and enl.
1217   ed., Kluwer Academic Publishers, Dordrecht; Boston, 954 pp., 1997.
1218 Rauber, R. M. and Tokay, A.: An Explanation for the Existence of Supercooled Water at the Top
1219   of Cold Clouds, J. Atmos. Sci., 48, 1005–1023, https://doi.org/10.1175/1520-
1220   0469(1991)048<1005:AEFTEO>2.0.CO;2, 1991.
1221 Rosenow, A. A., Plummer, D. M., Rauber, R. M., McFarquhar, G. M., Jewett, B. F., and Leon,
1222   D.: Vertical Velocity and Physical Structure of Generating Cells and Convection in the
1223   Comma Head Region of Continental Winter Cyclones, J. Atmos. Sci., 71, 1538–1558,
1224   https://doi.org/10.1175/JAS-D-13-0249.1, 2014.
1225 Roy, P., Rauber, R. M., and Di Girolamo, L.: A Closer Look at the Evolution of Supercooled
1226   Cloud Droplet Temperature and Lifetime in Different Environmental Conditions with
1227   Implications for Ice Nucleation in the Evaporating Regions of Clouds, J. Atmos. Sci., 80,
1228   2481–2501, https://doi.org/10.1175/JAS-D-22-0239.1, 2023.
1229 Schnaiter, F. M.: Particle Habit Imaging and Polar Scattering Probe (PHIPS) IMPACTS, Dataset
1230   available online from the NASA Global Hydrometeorology Resource Center DAAC,
1231   Huntsville, Alabama, USA [data set],
1232   https://doi.org/10.5067/IMPACTS/PHIPS/DATA101, 2020.
1233 Stark, D., Colle, B. A., and Yuter, S. E.: Observed Microphysical Evolution for Two East Coast
1234   Winter Storms and the Associated Snow Bands, M. Weather Rev., 141, 2037–2057,
1235   https://doi.org/10.1175/MWR-D-12-00276.1, 2013.
1236 Thornhill, K. L.: Turbulent Air Motion Measurement System (TAMMS) IMPACTS, Dataset
1237   available online from the NASA Global Hydrometeorology Resource Center DAAC,
1238   Huntsville, Alabama, USA [data set],
1239   https://doi.org/10.5067/IMPACTS/TAMMS/DATA101, 2022.
1240 Thornhill, K. L., Anderson, B. E., Barrick, J. D. W., Bagwell, D. R., Friesen, R., and Lenschow,
1241   D. H.: Air Motion Intercomparison Flights during Transport and Chemical Evolution in
1242   the Pacific (TRACE-P)/ACE-ASIA, J. Geophys. Res.-Atmos., 108, 2002JD003108,
1243   https://doi.org/10.1029/2002JD003108, 2003.
1244 Waldstreicher, J. and Brodzik, S.: NOAA Sounding IMPACTS, Dataset available online from
1245   the NASA Global Hydrometeorology Resource Center DAAC, Huntsville, Alabama,
1246   USA [data set], https://doi.org/10.5067/IMPACTS/SOUNDING/DATA201, 2022.

1247   Williams, C. R.: How Much Attenuation Extinguishes mm-Wave Vertically Pointing Radar
1248   Return Signals?, Remote Sens., 14, 1305, https://doi.org/10.3390/rs14061305, 2022.
1249   Yang-Martin, M. and Bennett, R.: P-3 Meteorological and Navigation Data IMPACTS, Dataset
1250   available online from the NASA Global Hydrometeorology Resource Center DAAC,
1251   Huntsville, Alabama, USA [data set], https://doi.org/10.5067/IMPACTS/P3/DATA101,
1252   2022.
1253   Zaremba, T. J., Rauber, R. M., Heimes, K., Yorks, J. E., Finlon, J. A., Nicholls, S. D., Selmer, P.,
1254   McMurdie, L. A., and McFarquhar, G. M.: Cloud-Top Phase Characterization of
1255   Extratropical Cyclones over the Northeast and Midwest United States: Results from
1256   IMPACTS, J. Atmos. Sci., 81, 341–361, https://doi.org/10.1175/JAS-D-23-0123.1, 2024.
1257   Zhang, J., Howard, K., Langston, C., Vasiloff, S., Kaney, B., Arthur, A., Van Cooten, S.,
1258   Kelleher, K., Kitzmiller, D., Ding, F., Seo, D.-J., Wells, E., and Dempsey, C.: National
1259   Mosaic and Multi-Sensor QPE (NMQ) System: Description, Results, and Future Plans,
1260   B. Am. Meteorol. Soc., 92, 1321–1338, https://doi.org/10.1175/2011BAMS-D-11-
1261   00047.1, 2011.